Journal of Scientific Computing (2023) 95:18
https://doi.org/10.1007/s10915-023-02143-3

A Flux Reconstruction Stochastic Galerkin Scheme for Hyperbolic Conservation Laws

Tianbai Xiao[1] · **Jonas Kusch**[3] · **Julian Koellermeier**[4] · **Martin Frank**[2]

Received: 25 May 2022 / Revised: 15 December 2022 / Accepted: 31 January 2023 /
Published online: 21 February 2023

Abstract
The study of uncertainty propagation poses a great challenge to design high fidelity numerical methods. Based on the stochastic Galerkin formulation, this paper addresses the idea and implementation of the first flux reconstruction scheme for hyperbolic conservation laws with random inputs. High-order numerical approximation is adopted simultaneously in physical and random space, i.e., the modal representation of solutions is based on an orthogonal polynomial basis and the nodal representation is based on solution collocation points. Therefore, the numerical behaviors of the scheme in the (physical-random) phase space can be designed and understood uniformly. A family of filters is developed in multi-dimensional cases to mitigate the Gibbs phenomenon arising from discontinuities in both physical and random space. The filter function is switched on and off by the dynamic detection of discontinuous solutions, and a slope limiter is employed to preserve the positivity of physically realizable solutions. As a result, the proposed method is able to capture the stochastic flow evolution where resolved and unresolved regions coexist. Numerical experiments including a wave propagation, a Burgers' shock, a one-dimensional Riemann problem, and a two-dimensional shock-vortex interaction problem are presented to validate the current scheme. The order of convergence of the high-order scheme is identified. The capability of the scheme for simulating smooth and discontinuous stochastic flow dynamics is demonstrated. The open-source codes to reproduce the numerical results are available under the MIT license (Xiao et al. in FRSG: stochastic Galerkin method with flux reconstruction. https://github.com/CSMMLab/FRSG, (2021). https://doi.org/10.5281/zenodo.5588317).

Keywords Computational fluid dynamics · High-order methods · Flux reconstruction · Uncertainty quantification · Stochastic Galerkin

✉ Tianbai Xiao
tianbaixiao@gmail.com

1 State Key Laboratory of High Temperature Gas Dynamics, Institute of Mechanics, Chinese Academy of Sciences, Beijing, China

2 Steinbuch Centre for Computing, Karlsruhe Institute of Technology, Karlsruhe, Germany

3 Institute of Mathematics, University of Innsbruck, Innsbruck, Austria

4 Bernoulli Institute for Mathematics, Computer Science and Artificial Intelligence, University of Groningen, Groningen, Netherlands

1 Introduction

The burgeoning research in uncertainty quantification (UQ) has facilitated applications in meteorology, particle physics, chemistry, bioinformatics, etc. [49]. In this paper, we focus on the propagation of randomness in stochastic hyperbolic conservation laws, i.e.,

$$\begin{aligned} &\partial_t \mathbf{u}(t,\mathbf{x},\mathbf{z}) + \nabla \cdot \mathbf{f}(\mathbf{u}(t,\mathbf{x},\mathbf{z})) = \mathbf{0}, \quad t \in (0,T],\ \mathbf{x} \in \boldsymbol{\Omega},\ \mathbf{z} \in \boldsymbol{\Upsilon}, \\ &\mathcal{B}(\mathbf{u}) = 0, \quad t \in (0,T],\ \mathbf{x} \in \partial\boldsymbol{\Omega},\ \mathbf{z} \in \boldsymbol{\Upsilon}, \\ &\mathbf{u}(0,\mathbf{x},\mathbf{z}) = \mathbf{u}_0, \quad \mathbf{x} \in \boldsymbol{\Omega},\ \mathbf{z} \in \boldsymbol{\Upsilon}, \end{aligned} \tag{1}$$

where $\mathbf{u}$ denotes the conservative variables, $\mathbf{f}$ is the flux function, $T \in \mathbb{R}^+$ is the evolution time, $\boldsymbol{\Omega} \subset \mathbb{R}^d$ is the physical space of dimension d, $\boldsymbol{\Upsilon} \subset \mathbb{R}^l$ is the random space of dimension l, and $\mathcal{B}$ is the boundary operator.

The stochastic Galerkin (SG) method has been successfully applied to solve the hyperbolic equations with random inputs. Compared with sampling-based methodologies, e.g., the Monte Carlo method and its variants [24], the SG method works in an intrusive way such that the original governing system in Eq. (1) is reformulated. Specifically, a set of generalized polynomial chaos (gPC) with respect to random variables is introduced, and the stochastic solution is approximated by the sum of the products between each modal coefficient and the corresponding orthogonal polynomial basis. Such an approach is generally referred to as the modal approximation. In contrast, the nodal approach directly employs collocation points in random space and fits the stochastic solution using interpolating polynomials, e.g., the Lagrange polynomials. As the residual of the governing equations is orthogonal to the linear space spanned by the polynomial chaos, the spectral convergence can be achieved provided that the solution depends smoothly on the random parameters [67].

Most stochastic Galerkin methods that have been applied to solve Eq. (1) employ finite difference or finite volume methods to discretize the gPC coefficients [27, 29, 30, 35, 44, 48, 60, 64]. Although this has proven to be an effective strategy, the different discretization strategies, i.e., the finite difference in physical space and the spectral representation in random space, make it indirect to understand the behavior of the numerical scheme in a uniform way. Most of the above methods hold no more than second order of accuracy. It has been noted in [41, 43] that the spatial discretization has significant effects on the solution quality in random space. The diffusive behavior of low-order methods can heavily smear out the solution. While it is possible to develop higher-order methods based on the finite difference or finite volume framework, the lack of ability to handle irregular geometry in the finite difference method and the non-compact stencils used in the traditional finite volume method prevent such extensions from being universally applicable [59].

The inherited high resolution and low dissipation of higher-order computational methods enable high-fidelity simulation of intricate flows in turbulence, acoustics and magnetohydrodynamics [3]. It motivates a unified spectral discretization for the stochastic Galerkin system, which leads to compatible accuracy in stochastic and spatial domain. This has been realized in [50, 68] for stochastic Navier-Stokes equations. However, in a hyperbolic system, discontinuous solutions can emerge from a smooth initial field, and the well-known Gibbs phenomenon brings tremendous challenges for spectral methods to capture the discontinuities in both physical and random space. To the best of the authors' knowledge, only a few research groups have addressed this issue following the discontinuous Galerkin (DG) approach [10, 25]. Dürrwächter et. al. [18, 19] developed a discontinuous stochastic Galerkin method for stochastic fluid dynamic equations. Donoghue and Yano [17] proposed a similar

methodology, while the focus is on the adaptive refinement of spatial mesh or polynomial chaos to control the numerical error.

The success of DG methods is attributed to the unified consideration of the spatial discretization and the spectral decomposition. Within each element, the solutions are approximated by polynomials and are allowed to be discontinuous across cell boundaries, which encourages the capturing of sharp structures that arise in hyperbolic systems. Based on similar views, the flux reconstruction (FR) approach proposed by Huynh et al. [28, 57] provides profound insight into constructing high-order methods for transport equations. It establishes a universal framework, where several existing approaches, including the nodal DG and the spectral difference (SD) [33, 39] methods, can be cast within by choosing different correction fields of Lagrange polynomials. The intrinsic connections between FR and DG or SD methods have been analyzed in [11, 14].

It is desirable to design the solution algorithm that equips consistent accuracy in time, space, and random domain for stochastic conservation laws. In this paper, we employ the flux reconstruction methodology as building blocks and develop the high-order stochastic Galerkin method for hyperbolic conservation laws. A family of multi-dimensional filters is developed to mitigate the oscillating solutions around discontinuities in the physical-random space. The filter function is dynamically dispatched based on a detector of discontinuous solutions to optimize the numerical dissipation. A slope limiter is applied to the nodal solutions to ensure the positivity of physically realizable solutions (e.g., the density and temperature in the Euler equations). The proposed algorithm can be understood uniformly as a spectral method within modal expansions and as a collocation method upon nodal solution points. The discontinuity capturing strategy is naturally incorporated into the solution algorithm based on the nodal-modal transformation. As a result, the proposed method is able to capture the stochastic fluid dynamics where resolved and unresolved regions coexist inside a flow field.

The rest of the paper is structured as follows. Section 2 introduces the generalized polynomial chaos and stochastic Galerkin formulation of hyperbolic conservation laws. Section 3 presents the implementation of the flux reconstruction framework. Section 4 expounds the strategy for capturing discontinuous solutions using filters. Section 5 includes the numerical experiments to demonstrate the performance of the new scheme. The paper ends with a short conclusion. Table 13 provides the nomenclature in this paper. The source codes to produce the numerical results are hosted on GitHub and distributed under the MIT license [65].

2 Stochastic Galerkin Method

2.1 Formulation

The stochastic Galerkin method employs the generalized polynomial chaos (gPC) expansion to describe the evolution of stochastic solutions. Defining the gPC polynomials up to degree N_c as $\Phi_k : \Upsilon \to \mathbb{R}$ where $|k| \le N_c$, a spectral representation of degree N_c is introduced in the random space as

$$\mathbf{u}(t,\mathbf{x},\mathbf{z}) \simeq \mathbf{u}^{N_c}(t,\mathbf{x},\mathbf{z}) = \sum_{|k|=0}^{N_c} \hat{\mathbf{u}}_k(t,\mathbf{x})\Phi_k(\mathbf{z}) = \hat{\mathbf{v}}(t,\mathbf{x})\boldsymbol{\Phi}(\mathbf{z}). \tag{2}$$

Here, $\hat{\mathbf{u}}_k = (\hat{u}_{1k}, \hat{u}_{2k}, \cdots, \hat{u}_{Sk})^T$ are the expansion coefficients of conservative variables in the polynomial chaos, and can also be called moments of the stochastic Galerkin system. The number of states in the solution vector is equal to S, which takes unit value for scalar

conservation laws. The index k can be a scalar or a l-dimensional vector $k = (k_1, k_2, \cdots, k_l)^T$ with $|k| = k_1 + k_2 + \cdots + k_l$. The matrix $\hat{\boldsymbol{v}} = \{\hat{\mathbf{u}}_k, |k| \leq N_c\}$ denotes a collection of the gPC coefficients at all orders.

The orthogonal polynomial basis $\boldsymbol{\Phi}$ satisfies the following constraints,

$$\mathbb{E}[\Phi_j(\mathbf{z})\Phi_k(\mathbf{z})] = \delta_{jk}, \quad 0 \leq |j|, |k| \leq N_c. \tag{3}$$

The expected value defines a scalar product,

$$\mathbb{E}[\Phi_j(\mathbf{z})\Phi_k(\mathbf{z})] = \int_{\boldsymbol{\Upsilon}} \Phi_j(\mathbf{z})\Phi_k(\mathbf{z})\varrho(\mathbf{z})d\mathbf{z}, \tag{4}$$

where $\varrho(\mathbf{z}) : \boldsymbol{\Upsilon} \to [0, \infty)$ is the probability density function. In practice, the above integral can be evaluated analytically or with the help of a numerical N_q-point quadrature rule, i.e.,

$$\mathbb{E}[\Phi_j(\mathbf{z})\Phi_k(\mathbf{z})] = \sum_{q=1}^{N_q} \Phi_j(\mathbf{z}_q)\Phi_k(\mathbf{z}_q)w(\mathbf{z}_q), \tag{5}$$

where $w(\mathbf{z}_q)$ is the corresponding quadrature weight function in random space. In the following we adopt a uniform notation $\mathbb{E}[\Phi_j(\mathbf{z})\Phi_k(\mathbf{z})] = \langle \Phi_j \Phi_k \rangle$ to denote the integrals over random space from Eq. (4) and (5).

Plugging Eq. (2) into Eq. (1) and projecting the resulting residuals to zero in the space spanned by the gPC basis, we get the conservation laws in the stochastic Galerkin formulation,

$$\begin{aligned} &\partial_t \hat{\mathbf{u}}_k + \langle \nabla \cdot \mathbf{f}\left(\mathbf{u}^{N_c}\right)\Phi_k \rangle = \mathbf{0}, \quad t \in (0, T], \ \mathbf{x} \in \boldsymbol{\Omega}, \\ &\langle \mathcal{B}(\mathbf{u}^{N_c})\Phi_k \rangle = 0, \quad t \in (0, T], \ \mathbf{x} \in \partial\boldsymbol{\Omega}, \\ &\hat{\mathbf{u}}_k(t = 0, \mathbf{x}) = \langle \mathbf{u}_0(\mathbf{x}, \mathbf{z})\Phi_k \rangle, \quad \mathbf{x} \in \boldsymbol{\Omega}. \end{aligned} \tag{6}$$

The stochastic Galerkin approach provides a desirable accuracy for the smooth solution in random space, where the residual of the governing equations is orthogonal to the linear space spanned by the gPC polynomials [67].

2.2 Challenge

While the stochastic Galerkin method has been successfully applied to various settings, its application in hyperbolic problems faces two main challenges. First, the SG system for the gPC coefficients in Eq. (6) is not necessarily hyperbolic, leading to a possible breakdown of the numerical method [1, 45]. Strategies to preserve hyperbolicity of the SG system include the intrusive polynomial moment (IPM) method [15, 45], the Roe transformation method [22, 23, 44], the operator splitting method [8, 9], the corrective reconstruction method [12, 13], and the hybrid stochastic Galerkin-collocation method [70]. Moreover, a so-called hyperbolicity-preserving limiter has been proposed [18, 48] which guarantees the realizability of the solution. That is, the limiter enforces positive density, pressure and energy. The IPM method is a generalization of stochastic Galerkin, which performs the gPC expansion on the entropy variables instead of the original conservative variables. Similarly, the Roe transformation method performs the expansion on the Roe variables. The hyperbolicity-preserving SG method employs a bound-preserving limiter to enforce positive moments of thermodynamic variables.

The second challenge is that the modal approximation suffers from the Gibbs phenomenon when the solution exhibits sharp gradients [38]. Strategies to mitigate spurious artifacts

from the Gibbs phenomenon in the random space have recently been developed. The multi-element SG method [53, 58] utilizes h-refinement in the random space, which is less prone to oscillations. The filtered SG and IPM methods are proposed in [2, 35], where a filtering step is applied to the solution in between time steps. In addition, stochastic adaptivity [4, 37, 40, 54] can be employed to increase the truncation order in oscillatory regions. For the IPM method, certain choices of the entropy mitigate oscillations [34]. It is a natural idea to combine different strategies for a better control of the numerical accuracy. As an example, in [36] the multi-element approach is extended to IPM and a filter step is performed after applying the bound-preserving limiter, which reduces the oscillations while maintaining realizability. A strategy of picking a sufficiently strong filter strength to preserve physical bounds of the solution is proposed in [63].

An important property of numerical methods for uncertainty quantification is the physical realizablity (e.g., the positivity of certain thermodynamic variables). It is desirable to consider the realizability and mitigation of the Gibbs phenomenon uniformly in the solution algorithm. In this paper, we will develop the multi-dimensional filter and limiter respectively that can mitigate spurious artifacts from the Gibbs phenomenon in both physical and random space and ensure the realizability of physical solutions. The detailed strategy will be illustrated in Sect. 4.

3 Flux Reconstruction Framework

3.1 Formulation

Considering N_x non-overlapping cells in the domain $\boldsymbol{\Omega} = \bigcup_{i=1}^{N_x} \boldsymbol{\Omega}_i$, we approximate the solution of the conservation laws with piecewise polynomials, i.e.,

$$\mathbf{u} \approx \bigoplus_{i=1}^{N_x} \hat{\boldsymbol{v}}_i \boldsymbol{\Phi}, \quad \mathbf{f} \approx \bigoplus_{i=1}^{N_x} \hat{\boldsymbol{f}}_i \boldsymbol{\Phi}. \tag{7}$$

For convenience, the standard element in the reference space can be introduced based on the transformation of coordinates,

$$\mathbf{x}_i = \boldsymbol{\Theta}_i(\mathbf{r}) = \sum_{j=1}^{N_v} \chi_j(\mathbf{r}) \mathbf{x}_{i,j}, \tag{8}$$

where $\{\mathbf{x}, \mathbf{r}\}$ represent the global and local coordinates of a point in the element $\boldsymbol{\Omega}_i$. These two coordinates can be connected by the vertex coordinates χ_j, which are built upon N_v vertices and their global coordinates $\mathbf{x}_{i,j}$. For elements of different shapes, the vertex coordinates take different forms, e.g.,

$$\chi_1 = \frac{1-r}{2}, \ \chi_2 = \frac{1+r}{2}, \tag{9}$$

in one-dimensional line elements,

$$\chi_1 = -\frac{r+s}{2}, \ \chi_2 = \frac{r+1}{2}, \ \chi_3 = \frac{s+1}{2}, \tag{10}$$

in isosceles right triangle elements where $\mathbf{r} = (r, s)^T$, and the bi-linear rectangle shape functions,

$$\begin{aligned} \chi_1 &= \frac{(r-1)(s-1)}{4}, \quad \chi_2 = \frac{(r+1)(1-s)}{4}, \\ \chi_3 &= \frac{(r+1)(s+1)}{4}, \quad \chi_4 = \frac{(1-r)(s+1)}{4}, \end{aligned} \tag{11}$$

in square elements.

Therefore, the stochastic Galerkin conservation laws in the reference space read

$$\frac{\partial \hat{\boldsymbol{v}}^{\delta}}{\partial t} = -\nabla_{\mathbf{r}} \cdot \hat{\boldsymbol{f}}^{\delta}, \tag{12}$$

where $\hat{\boldsymbol{v}}^{\delta}$ denotes the matrix of all the gPC coefficients in the reference space, and $\hat{\boldsymbol{f}}^{\delta}$ are the numerical fluxes, which we will derive in the following.

3.2 Discontinuous Flux

In the flux reconstruction method, the solution is approximated by piecewise polynomials in physical space. For brevity, we consider a one-dimensional geometry first to illustrate the solution algorithm. Defining the Lagrange polynomials based on N_p solution points,

$$\ell_j = \prod_{k=1, k\neq j}^{N_p} \left(\frac{r - r_k}{r_j - r_k} \right), \tag{13}$$

the conservative variables in the element Ω_i can be represented as,

$$\hat{\boldsymbol{v}}^{\delta}(t, r) = \sum_{j=1}^{N_p} \hat{\boldsymbol{v}}^{\delta}(t, r_j)\ell_j(r). \tag{14}$$

The fluxes at these solution points can then be determined and transformed via

$$\hat{\boldsymbol{f}}^{\delta D}(t, r) = \frac{\hat{\boldsymbol{f}}\left(\hat{\boldsymbol{v}}\left(t, \boldsymbol{\Theta}_i(r)\right)\right)}{J_i}, \tag{15}$$

where $\hat{\boldsymbol{f}}$ is the flux function related to the specific governing equations, and $J_i = (x_{i+1/2} - x_{i-1/2})/2$ is the Jacobian of coordinate transformation. Therefore, the flux polynomials can be constructed as,

$$\hat{\boldsymbol{f}}^{\delta D}(t, r) = \sum_{j=1}^{N_p} \hat{\boldsymbol{f}}^{\delta D}(t, r_j)\ell_j(r), \tag{16}$$

where $\hat{\boldsymbol{f}}^{\delta D}(t, r_j)$ denotes the evaluated flux calculated by Eq. (15) at solution point r_j and time t. The notation δD implies that such a flux is basically discontinuous since it is derived directly from piecewise discontinuous solutions $\hat{\boldsymbol{v}}^{\delta}$.

3.3 Interactive Flux

It is noticeable that the discontinuous flux polynomials in Eq. (15) are of the same degree of freedom $N_p - 1$ as numerical solutions. A direct application of the derivatives of Eq. (15) directly to solve Eq. (12) results in erroneous results since such a treatment does not take the information from adjacent cells into consideration and can by no means deal with boundary conditions. A key ingredient of the flux reconstruction method is to introduce a correction term of degree N_p to the transformed discontinuous fluxes, i.e.,

$$\hat{\boldsymbol{f}}^{\delta} = \hat{\boldsymbol{f}}^{\delta D} + \hat{\boldsymbol{f}}^{\delta C}. \tag{17}$$

The total fluxes are expected to equal the correct interactive fluxes at cell boundaries, and to preserve similar in-cell profiles of discontinuous fluxes. A feasible approach, as proposed in [28], is to introduce two symmetric auxiliary functions $\{h_L, h_R\}$, which satisfy the following restrictions,

$$\begin{aligned} &h_L(r) = h_R(-r), \\ &h_L(-1) = 1,\ h_R(-1) = 0, \\ &h_L(1) = 0,\ h_R(1) = 1. \end{aligned} \tag{18}$$

The corresponding corrective flux can then be reconstructed as

$$\hat{\boldsymbol{f}}^{\delta C} = (\hat{\boldsymbol{f}}_L^{\delta I} - \hat{\boldsymbol{f}}_L^{\delta D})h_L + (\hat{\boldsymbol{f}}_R^{\delta I} - \hat{\boldsymbol{f}}_R^{\delta D})h_R. \tag{19}$$

Here $\{\hat{\boldsymbol{f}}_L^{\delta D}, \hat{\boldsymbol{f}}_R^{\delta D}\}$ are the reconstructed discontinuous fluxes from the Lagrange interpolation at the left and right boundary of the element, and $\{\hat{\boldsymbol{f}}_L^{\delta I}, \hat{\boldsymbol{f}}_R^{\delta I}\}$ are the interactive fluxes at the boundaries. Such fluxes can be obtained by nonlinear flux solvers, e.g. the Lax-Friedrichs and Roe's method [52]. Note that by choosing specific correction functions $\{h_L, h_R\}$, the flux reconstruction method can recover different numerical schemes [57]. For example, recovery of the nodal discontinuous Galerkin scheme requires the use of Radau polynomials defined as

$$h_L = \frac{(-1)^k}{2}(L_k - L_{k+1}), \quad h_R = \frac{1}{2}(L_k + L_{k+1}), \tag{20}$$

where L_k is the Legendre polynomial of degree k. If the correction functions are defined as

$$\begin{aligned} h_L &= \frac{(-1)^k}{2}\left[L_k - \left(\frac{kL_{k-1} + (k+1)L_{k+1}}{2k+1}\right)\right], \\ h_R &= \frac{1}{2}\left[L_k + \left(\frac{kL_{k-1} + (k+1)L_{k+1}}{2k+1}\right)\right], \end{aligned} \tag{21}$$

then the spectral difference scheme can be recovered. A detailed derivation of the equivalence can be found in [28]. Note that changing the correction function can have a noticeable effect on the numerical property of the flux reconstruction method. The criteria for choosing the correction function and building the scheme from it are the stability and accuracy based on approximation theory and Fourier analysis. However, such options can still be varied as different schemes are able to meet the stability and accuracy requirements. Although there has been some work comparing the numerical schemes recovered from the FR method [69], it is very difficult to derive an optimal scheme since such a scheme is likely to be problem dependent. In this paper, we mainly focus on the Radau polynomials defined to recover the nodal DG scheme with random inputs.

3.4 Total Flux

Given the total flux $\hat{\boldsymbol{f}}^{\delta}$, its derivatives can be expressed as

$$\frac{\partial \hat{\boldsymbol{f}}^{\delta}}{\partial r} = \frac{\partial \hat{\boldsymbol{f}}^{\delta D}}{\partial r} + \frac{\partial \hat{\boldsymbol{f}}^{\delta C}}{\partial r}. \tag{22}$$

It can be evaluated by calculating the divergences of the Lagrange polynomials and the corrective functions at each solution point r_j, i.e.,

$$\frac{\partial \hat{\boldsymbol{f}}^{\delta}}{\partial r}(r_j) = \sum_{k=1}^{N_p} \hat{\boldsymbol{f}}_k^{\delta D} \frac{\mathrm{d}\ell_k}{\mathrm{d}r}(r_j) + \left(\hat{\boldsymbol{f}}_L^{\delta I} - \hat{\boldsymbol{f}}_L^{\delta D}\right) \frac{\mathrm{d}h_L}{\mathrm{d}r}(r_j) + \left(\hat{\boldsymbol{f}}_R^{\delta I} - \hat{\boldsymbol{f}}_R^{\delta D}\right) \frac{\mathrm{d}h_R}{\mathrm{d}r}(r_j). \tag{23}$$

Till now, we have completed the construction of the right-hand side of the governing equations. Appropriate numerical integrators can be chosen to compute the time-marching solutions.

3.5 Multi-dimensional Extension

The above flux reconstruction procedures can be extended to multi-dimensional cases. Inside the element $\boldsymbol{\Omega}_i$, we approximate the solutions as,

$$\hat{\boldsymbol{v}}^{\delta}(t, \mathbf{r}) = \sum_{j=1}^{N_p} \hat{\boldsymbol{v}}_j^{\delta}(t) \ell_j(\mathbf{r}), \tag{24}$$

where $\ell_j(\mathbf{r})$ denotes the the multi-dimensional Lagrange polynomials, and N_p is the number of solution points. If tensorized elements are considered, the above expansion can be simplified as the product of one-dimensional Lagrange polynomials. For example, in a quadrilateral element, the solution expansion takes the form,

$$\hat{\boldsymbol{v}}^{\delta}(t, r, s) = \sum_{j=1}^{\sqrt{N_p}} \sum_{k=1}^{\sqrt{N_p}} \hat{\boldsymbol{v}}_{j,k}^{\delta}(t) \ell_j(r) \ell_k(s), \tag{25}$$

where $\mathbf{r} = (r, s)$. The Lagrange polynomials in a generic element can be evaluated by the nodal-modal transformation with the help of the Vandermonde matrix [25]. Therefore, the right-hand side of the governing equation in the flux reconstruction formulation becomes

$$\begin{aligned} \frac{\partial \hat{\boldsymbol{v}}^{\delta}}{\partial t}(\mathbf{r}_j) &= -\nabla_{\mathbf{r}} \cdot \hat{\boldsymbol{F}}^{\delta}(\mathbf{r}_j) \\ &= \sum_{k=1}^{N_p} \hat{\boldsymbol{F}}_k^{\delta D} \cdot \nabla_{\mathbf{r}} \ell_k(\mathbf{r}_j) + \sum_{f=1}^{N_f} \sum_{k=1}^{N_{fp}} \left[\left(\hat{\boldsymbol{F}}_{f,k}^{I} - \hat{\boldsymbol{F}}_{f,k}^{\delta D}\right) \cdot \mathbf{n}_{f,k}^{\delta}\right] \nabla_{\mathbf{r}} \cdot \mathbf{h}_{f,k}(\mathbf{r}_j). \end{aligned} \tag{26}$$

where N_f is the number of faces and N_{fp} is the number of flux points at each face. The flux tensor takes $\hat{\boldsymbol{F}}^{\delta} = (\hat{\boldsymbol{f}}^{\delta}, \hat{\boldsymbol{g}}^{\delta})$ in the two-dimensional case and $\hat{\boldsymbol{F}}^{\delta} = (\hat{\boldsymbol{f}}^{\delta}, \hat{\boldsymbol{g}}^{\delta}, \hat{\boldsymbol{h}}^{\delta})$ in the three-dimensional case. The unit normal vector $\hat{\mathbf{n}}_{f,k}$ points outwards of the element. The corrective function $\mathbf{h}_{f,k}$ at k-th flux point of f-th face is a vector, which satisfies the following constraints,

$$\mathbf{h}_{f,k}\left(\mathbf{r}_{j,l}\right)\cdot\mathbf{n}_{j,l}^{\delta}=\begin{cases}1, & \text{if } f=j \text{ and } k=l,\\ 0, & \text{if } f\neq j \text{ or } k\neq l.\end{cases} \tag{27}$$

In this paper, since our focus is on the combination of the flux reconstruction and stochastic Galerkin methods, we consider a classical setting that makes use of the maximal order polynomial basis. Note that the use of the Euclidean order basis may help reduce the computational cost of the flux reconstruction method in two- and three-dimensional cases [25].

4 Discontinuity Capturing Strategy

In this section, we present the detailed strategy for capturing discontinuous solutions robustly and maintaining the realizability of the solution. A series of filters that can be applied in the multi-dimensional physical-random space is introduced to reduce the Gibbs phenomenon. A detector of discontinuity is employed to adapt numerical dissipation based on local flow conditions and maintain the optimal accuracy. Besides, a positivity-preserving limiter is built to enforce the realizability of physical solutions.

For convenience of the illustration, we introduce the following transformation between nodal and modal representations of solutions. Inside any element $\boldsymbol{\Omega}_i$, the solutions can be expressed as,

$$\begin{aligned}\mathbf{u}_i^{\delta}\simeq\mathbf{u}_i^{N}&=\sum_{j=1}^{N_p}\sum_{k=0}^{N_c}\hat{\mathbf{u}}_{i,j,k}^{\delta}\ell_j\Phi_k\\&=\tilde{\mathbf{u}}_i^{N}=\sum_{j=0}^{N_p-1}\sum_{k=0}^{N_c}\tilde{\mathbf{u}}_{i,j,k}^{\delta}\Psi_j\Phi_k.\end{aligned} \tag{28}$$

The first line in Eq. (28) approximates the gPC coefficients of the stochastic solutions by constructing Lagrange polynomials from collocation points in physical space, which we call the nodal representation. The second line adopts a spectral representation with the help of orthogonal polynomials in physical space, which we refer as the modal representation. Here Ψ_j and Φ_k denote the orthogonal polynomials in reference physical and random space, with degrees N_p-1 and N_c, respectively. The nodal and modal representations of gPC coefficients are related by the Vandermonde matrix,

$$\mathcal{V}\hat{\mathbf{v}}_i^{\delta}=\tilde{\mathbf{v}}_i^{\delta}, \tag{29}$$

where $\hat{\mathbf{v}}_i^{\delta}=\{\hat{\mathbf{u}}_{i,j,k}^{\delta},1\le|j|\le N_p,|k|\le N_c\}$ and $\tilde{\mathbf{v}}_i^{\delta}=\{\tilde{\mathbf{u}}_{i,j,k}^{\delta},|j|\le N_p-1,|k|\le N_c\}$ denote the matrices of gPC coefficients in $\mathbf{u}_i^N$ and $\mathbf{u}_i^N$ respectively, and the entries of the Vandermonde matrix write,

$$\mathcal{V}_{jk}=\Psi_k(\mathbf{r}_j). \tag{30}$$

4.1 Filter

4.1.1 Exponential Filter

The idea of filtering is to dampen the coefficients in the polynomial expansions. Such damping effect is expected to vanish as the expansion term approaches infinity in the sense of consistency. The exponential filter is arguably the most widely used filter for spectral methods [25,

26]. It was recently used to reduce oscillations and increase convergence speed in kinetic equations [16, 20] as well as uncertainty quantification [2, 36]. Given a one-dimensional modal solution $\tilde{\mathbf{u}}^N$, the exponential filtering takes the form

$$\mathbf{u}^* = \mathcal{F}(\tilde{\mathbf{u}}^N) = \sum_{k=0}^{N} \lambda_k \tilde{\mathbf{u}}_k^\delta \Phi_k, \tag{31}$$

where $\mathbf{u}^*$ is the post-filter solution. The filter strength λ is defined as,

$$\lambda_k\left(\eta = \frac{k}{N}\right) = \begin{cases} 1, & 0 \le \eta < \eta_* = \frac{N^*}{N}, \\ \exp\left(-\alpha \Delta t \left((\eta - \eta_*)/(1-\eta_*)\right)^s\right), & \eta_* \le \eta \le 1. \end{cases} \tag{32}$$

Here, $N^* \ge 0$ represents a cutoff below which the modes are left untouched, e.g., $N^* = \frac{2}{3}N$ as recommended by [26]. The exponent s is an integer to be determined in specific examples, with $s = 36$ in [26, 31]. The filter parameter $\alpha \ge 0$ is chosen as $\alpha = 36$ in [26] to ensure that the last mode is fully damped up to machine precision. The choice of α largely depends on the application and several ways to choose appropriate filter parameters are discussed in detail in [20]. We refer to Appendix A for more details and a parameter study of the filter as used in this work. The necessary parameter choices are an apparent drawback of the exponential filter but also allow for some flexibility in applications.

The filter operator $\mathcal{F}$ can be written as,

$$\mathcal{F}(\tilde{\mathbf{u}}^N) = \lambda \circ \tilde{\mathbf{u}}^N, \tag{33}$$

where $\lambda = [\lambda_0, \lambda_1, \cdots, \lambda_N]^T$.

The above filter can be extended to multi-variate modal solutions in Eq. (28), i.e.,

$$\begin{aligned} \mathbf{u}^* = \mathcal{F}(\mathbf{u}^N) &= \sum_{j=0}^{N_p-1} \sum_{k=0}^{N_c} \lambda_{j,k} \tilde{\mathbf{u}}_{j,k}^\delta \Psi_j \Phi_k, \\ \lambda_{j,k}\left(\eta_1 = \frac{j}{N_p}, \eta_2 = \frac{k}{N_c+1}\right) &= \begin{cases} 1, & 0 \le \eta < \eta_{*,\{1,2\}}, \\ \prod_{i=1}^{2} \exp\left(-\alpha \Delta t \left(\left(\eta_i - \eta_{*,i}\right)/\left(1-\eta_{*,i}\right)\right)^s\right), & \text{else}, \end{cases} \end{aligned} \tag{34}$$

where $\eta_{*,1} = \frac{N_*}{N_p}$ and $\eta_{*,2} = \frac{N_*}{N_c+1}$. Note that also the filter parameter and exponent can be made dependent on the dimension. The filter operator can be abbreviated again as,

$$\mathcal{F} = \Lambda \circ, \tag{35}$$

where the $\lambda_{j,k}$ are the entries of the matrix Λ. It is noticeable that the filter operator can act on the nodal solution directly in practice, where the equivalent filter operator becomes,

$$\mathcal{F}^* = \mathcal{V} \Lambda \circ \mathcal{V}^{-1}, \tag{36}$$

where $\mathcal{V}$ is the Vandermonde matrix defined in Eq. (30).

4.1.2 L^2 Filter

As the spectral solution is dedicated to approximating the exact solution $\mathbf{u}^\delta$, we can define the discrepancy between the approximation and the exact solutions based on the norms of

the solution matrix. For example, the cost function of the L^2 norm can be written as,

$$\mathcal{C}(\mathbf{u}^N) := \frac{1}{V}\int_{\boldsymbol{\Omega}}\int_{\boldsymbol{\Upsilon}} \left\|\mathbf{u}^\delta - \tilde{\mathbf{u}}^N\right\|_{L^2}^2 \varrho(\mathbf{r})\varrho(\mathbf{z})d\mathbf{r}d\mathbf{z}, \tag{37}$$

where V is the volume of the phase space and ϱ denotes the probability density in the spatial and random domains.

The L^2 filter based on splines [7] regularizes the above error to mitigate oscillations. A penalty term can be introduced into Eq. (37),

$$\begin{aligned}\mathcal{C}_\alpha(\mathbf{u}^N) := \frac{1}{V}\int_{\boldsymbol{\Omega}}\int_{\boldsymbol{\Upsilon}} &\left\|\mathbf{u}^\delta - \sum_{j=0}^{N_p-1}\sum_{k=0}^{N_c}\tilde{\mathbf{u}}_{j,k}^\delta \Psi_j\Phi_k\right\|_{L^2}^2 \varrho(\mathbf{r})\varrho(\mathbf{z})d\mathbf{r}d\mathbf{z}\\ &+\int_{\boldsymbol{\Omega}}\int_{\boldsymbol{\Upsilon}} \left\|\alpha_1\mathcal{L}_1\sum_{j=0}^{N_p-1}\sum_{k=0}^{N_c}\tilde{\mathbf{u}}_{j,k}^\delta \Psi_j\Phi_k\right.\\ &\left.+\alpha_2\mathcal{L}_2\sum_{j=0}^{N_p-1}\sum_{k=0}^{N_c}\tilde{\mathbf{u}}_{j,k}^\delta \Psi_j\Phi_k\right\|_{L^2}^2 \varrho(\mathbf{r})\varrho(\mathbf{z})d\mathbf{r}d\mathbf{z},\end{aligned} \tag{38}$$

where the operator $\mathcal{L}$ is used to punish the possible oscillations and $\alpha_{1,2} \in \mathcal{R}^+$ are the filter parameters. A common choice of the penalty operator is

$$\mathcal{L}_i u(\boldsymbol{y}) = \partial_{y_i}\left((1-y_i^2)\partial_{y_i}u(\boldsymbol{y})\right), \tag{39}$$

where $\boldsymbol{y} = (y_1, \cdots, y_M)$ is an arbitrary vector-valued input. Note that the Legendre polynomials are eigenfunctions of this operator. Differentiating Eq. (38) with respect to the L^2 norm yields the optimal coefficients,

$$\mathbf{u}^* = \sum_{j=0}^{N_p-1}\sum_{k=0}^{N_c}\tilde{\mathbf{u}}_{j,k}^*\Psi_j\Phi_k, \quad \tilde{\mathbf{u}}_{j,k}^* = \frac{\tilde{\mathbf{u}}_{j,k}^\delta}{1+\alpha_1 j^2(j+1)^2+\alpha_2 k^2(k+1)^2}, \tag{40}$$

where $\hat{\mathbf{u}}_{j,k}^*$ denotes the coefficients after filtering. As can be seen, the filter leaves the zeroth-order coefficients untouched and thus preserve the conservation of the expected value.

The filter parameters $\{\alpha_1, \alpha_2\}$ have yet to be determined. If we specify the damping ratio of the last expansion term, the filter parameter can be obtained via,

$$\alpha_1 = \frac{1}{\varepsilon_1 N_p^2(N_p-1)^2}, \quad \alpha_2 = \frac{1}{\varepsilon_2 N_c^2(N_c+1)^2}, \tag{41}$$

where ε_1 and ε_2 denote the relative magnitudes of coefficients in the last expansion term with respect to spatial and random space. Usually $\{\varepsilon_1, \varepsilon_2\}$ take higher values than for the exponential filter, where the last expansion term is dampened towards zero. Furthermore, note that if N_p and N_c tend to infinity, the above choice of the filter parameter ensures convergence, as the filtering effect vanishes in the limit.

4.1.3 Lasso Filter

The cost function of the approximation solution can be defined on other norms, e.g., the L^1 norm. In [35], the filtering idea is combined with Lasso regression, and we can propose the

following cost function in multi-dimensional space,

$$\mathcal{C}_\alpha(\mathbf{u}^*) := \frac{1}{V}\int_{\boldsymbol{\Omega}}\int_{\boldsymbol{\Upsilon}} \left\|\mathbf{u}^\delta - \mathbf{u}^*\right\|_{L^2}^2 \varrho(\mathbf{r})\varrho(\mathbf{z}) d\mathbf{r}d\mathbf{z} + \frac{1}{V}\int_{\boldsymbol{\Omega}}\int_{\boldsymbol{\Upsilon}} \sum_{j=1}^{N_p-1}\sum_{k=1}^{N_c}\Big(\alpha_1 \left\|\mathcal{L}_1\tilde{\mathbf{u}}^*_{j,k}\Psi_{j,k}\right\|_{L^1} + \alpha_2 \left\|\mathcal{L}_2\tilde{\mathbf{u}}^*_{j,k}\Psi_{j,k}\right\|_{L^1}\Big)\varrho(\mathbf{r})\varrho(\mathbf{z}) d\mathbf{r}d\mathbf{z}, \tag{42}$$

where the penalty term is based on the L^1 norm and acts on the expansion term individually.

Conveniently, the above optimization problem has an analytic solution, therefore reducing computational costs significantly. The result follows from a straightforward extension of [35, Theorem 1]:

Theorem 1 *The minimizer of Eq. (42) takes the form*

$$\tilde{\mathbf{u}}^*_{j,k} = \mathrm{ReLU}\left(1 - \frac{\alpha_1 j(j+1)\|\Psi_j\Phi_k\|_{L^1}}{|\tilde{\mathbf{u}}^\delta_{j,k}|} - \frac{\alpha_2 k(k+1)\|\Psi_j\Phi_k\|_{L^1}}{|\tilde{\mathbf{u}}^\delta_{j,k}|}\right)\tilde{\mathbf{u}}^\delta_{j,k}, \tag{43}$$

where ReLU is the rectified linear unit function and $\|\cdot\|_{L^1}$ denotes the L^1 norm. The absolute value in the denominator is applied element-wise to the vector $\tilde{\mathbf{u}}^\delta_{j,k}$.

Proof For ease of presentation, we assume the solution to be scalar. The extension to the system case is trivial and can be found in [35, Theorem 1]. Let us denote potential minimizers by $\boldsymbol{\alpha} \in \mathbb{R}^{(N_p-1)\times N_c}$. To minimize the cost functional (42), we need to determine the gradient. Since the cost function is not smooth, Lasso regression relies on the subdifferential [51] instead of the gradient. The subdifferential with respect to the expansion coefficient $\alpha_{i,\ell}$ is denoted by $\partial_{i,\ell}\mathcal{C}_\alpha(\boldsymbol{v})$. When $v_{i,\ell} = 0$, we have

$$\partial_{i,\ell}\mathcal{C}_\alpha(\boldsymbol{v}) = \left\{c_{i,\ell}(\boldsymbol{v},\gamma) : \gamma \in [-1,1]\right\} \tag{44}$$

where with $\tilde{\varrho}(r,z) := \varrho(r)\varrho(z)$ and $u^\delta_{i\ell} := \int u^\delta \psi_i\phi_\ell\tilde{\varrho}\, drdz$ we have

$$\begin{aligned} c_{i,\ell}(\boldsymbol{v},\gamma) :=& \int\left(\sum_{j,k} v_{jk}\psi_j\phi_k - u^\delta\right)\psi_i\phi_\ell\tilde{\varrho}\, drdz \\ &+ \gamma\int\sum_{j,k}\left(\left|\alpha_1\mathcal{L}_1 v_{jk}\psi_j\phi_k\right| + \left|\alpha_2\mathcal{L}_2 v_{jk}\psi_j\phi_k\right|\right)\tilde{\varrho}\, drdz \\ =& v_{i\ell} - u^\delta_{i\ell} + \gamma\int\left(|\alpha_1 i(i+1)\psi_i\phi_\ell| + |\alpha_2\ell(\ell+1)\psi_i\phi_\ell|\right)\tilde{\varrho}\, drdz. \end{aligned} \tag{45}$$

To have optimality, we need $0 \in \partial_{i,\ell}\mathcal{C}_\alpha(\boldsymbol{v})$, i.e., if

$$u^\delta_{i\ell} \in \left[-\left(\alpha_1 i(i+1) + \alpha_2\ell(\ell+1)\right)\|\psi_i\phi_\ell\|_{L^1}, \left(\alpha_1 i(i+1) + \alpha_2\ell(\ell+1)\right)\|\psi_i\phi_\ell\|_{L^1}\right], \tag{46}$$

we must set $v_{i,\ell}$ to zero. If $u^\delta_{i\ell}$ does not fulfill Eq. (46), we know that $v_{i,\ell} \neq 0$ and the cost function is differentiable. Then, the gradient can be computed and the optimality condition is simply given by

$$\partial_{i,\ell}\mathcal{C}_\alpha(\boldsymbol{v}) = v_{i\ell} - u^\delta_{i\ell} + \mathrm{sign}(v_{i,\ell})\left(\alpha_1 i(i+1) + \alpha_2\ell(\ell+1)\right)\|\psi_i\phi_\ell\|_{L^1} \overset{!}{=} 0.$$

Hence, if (46) does not hold, we have

$$v_{i\ell} = u^{\delta}_{i\ell} - \text{sign}(v_{i,\ell})\,(\alpha_1 i(i+1) + \alpha_2 \ell(\ell+1))\,\|\psi_i \phi_\ell\|_{L^1}.$$

Following the proof of [35, Theorem 1], this can be written down compactly as Eq. (43). □

The Lasso filter yields an automated and adaptive strategy to pick an adequate filter parameter. Following [35], we wish to choose the filter parameter, such that no information is lost through the imposed polynomial truncation. A likely scenario which achieves this goal is when the filter sets the highest expansion coefficients to zero. To ensure that the filtered coefficients $\tilde{\mathbf{u}}^*_{N_p-1,0}$ and $\tilde{\mathbf{u}}^*_{0,N_c}$ are zero, this leads to,

$$\begin{aligned} \alpha_1 &= \frac{\|\tilde{\mathbf{u}}^{\delta}_{N_p-1,0}\|_{L^1}}{N_p(N_p-1)\|\Psi_{N_p-1}\Phi_0\|_{L^1}}, \\ \alpha_2 &= \frac{\|\tilde{\mathbf{u}}^{\delta}_{0,N_c}\|_{L^1}}{N_c(N_c+1)\|\Psi_0\Phi_{N_c}\|_{L^1}}. \end{aligned} \tag{47}$$

4.2 Discontinuity Detector

The filter functions are used globally each step or every few steps during the simulation. This may lead to a loss of accuracy in smooth regions, where the solution structure has been well captured by the polynomial expansions. A better strategy would be that appropriate numerical dissipation is injected only when it is needed. This requires a proper detection of discontinuous solutions. Here we follow the sensor for discontinuities proposed in [42] for the discontinuous Galerkin methods. The sensor has been used in [47] for the filtered stochastic-Galerkin method.

Let us consider the modal solution in the element $\boldsymbol{\Omega}_i$,

$$\mathbf{u}^N = \sum_{j=0}^{N_p-1}\sum_{k=0}^{N_c} \tilde{\mathbf{u}}^{\delta}_{j,k}\Psi_j\Phi_k, \tag{48}$$

where N_p is the number of solution points, and N_c is the degree of polynomial chaos in the random space. In the smooth region, the coefficients $\tilde{\mathbf{u}}^{\delta}_{j,k}$ are expected to decrease quickly with increasing polynomial order. Therefore, a slope indicator can be defined as

$$\mathbf{S}_e = \frac{\langle \mathbf{u}^N - \mathbf{u}^{N-1}, \mathbf{u}^N - \mathbf{u}^{N-1}\rangle}{\langle \mathbf{u}^N, \mathbf{u}^N\rangle}, \tag{49}$$

where $\mathbf{u}^{N-1}$ denotes a truncated expansion of the same solution at order $N-1$. The indicator $\mathbf{S}_e$ can be a non-negative number for scalar transport equations, or a vector for a system of equations. We extract the first state of $\mathbf{S}_e$ and define it as S_e. A discontinuity detector can be formulated as,

$$\theta = \begin{cases} 1, & s_e < s_0 - \kappa, \\ \frac{1}{2}\left(1 - \sin\frac{\pi(s_e - s_0)}{2\kappa}\right), & s_0 - \kappa \le s_e \le s_0 + \kappa, \\ 0, & s_e > s_0 + \kappa. \end{cases} \tag{50}$$

$$\theta < 0.99 \longrightarrow \text{discontinuity},$$

where $s_e = \log_{10}(S_e)$. The parameter s_0 is chosen to be inversely proportional to the polynomial degree, and κ needs to be sufficiently large to obtain a sharp and non-oscillating solution profile.

4.3 Positivity Preserving Limiter

The use of filters suffices to mitigate the Gibbs phenomenon and thus stabilizes the numerical computation. However, it does not necessarily preserve the realizability of physical solutions, e.g., the non-negative density and temperature in the Euler equations. A feasible strategy is to apply filters either with sufficiently strong filter parameter [2] or successively [63], but the excess introduction of artificial dissipation may cause a severe loss of accuracy or even destroy the physical structure. In this paper, we adopt a slope limiter in conjunction with the filter to preserve the positivity of realizable solutions. The idea of limiting the solution slopes comes naturally from the development of high-order methods, e.g., the discontinuous Galerkin method [5] and the flux reconstruction method [56]. We extend the limiter proposed in [56] to multi-dimensional spatial-random space. A similar strategy has been applied in [18], which extends the limiter in random space [48] under the DG framework.

For clarity, we take the Euler equations as an example. In the solution algorithm, we first evaluate the polynomial chaos at quadrature points in the random space,

$$\begin{aligned} \mathbf{u}_i^\delta \simeq \mathbf{u}_i^N &= \sum_{j=1}^{N_p} \sum_{k=0}^{N_c} \hat{\mathbf{u}}_{i,j,k}^\delta \ell_j \Phi_k \\ &= \check{\mathbf{u}}_i^N = \sum_{j=1}^{N_p} \sum_{k=1}^{N_c+1} \mathbf{u}_{i,j,k}^\delta \ell_j(r) \ell_k(z), \end{aligned} \tag{51}$$

where the fully nodal representation is denoted as $\check{\mathbf{u}}_i^N$.

For an interpolation higher than P_1, the local extrema of density and pressure can emerge at any point in the element, and thus we need to detect the minimum value among both solution points and flux points. Note that this step can be done together with the Lagrange interpolation for the interface flux calculation in Eq. (19). As we demand positivity of both density and pressure, the limiter is turned on when the following condition is satisfied,

$$\min(\rho_{\min}, p_{\min}) < \epsilon, \tag{52}$$

where the small parameter ϵ for the element $\boldsymbol{\Omega}_i$ is defined via,

$$\epsilon = \min(10^{-8}, \bar{\rho}_i, \bar{p}_i). \tag{53}$$

The mean density $\bar{\rho}_i$ and mean pressure $\bar{p}_i$ are calculated in each element $\boldsymbol{\Omega}_i$.

The density value at the j-th solution point in the physical space and the k-th quadrature point in the random space is then reconstructed with limited slopes as,

$$\rho_{i,j,k}^\star = \beta_1 \left(\rho_{i,j,k} - \bar{\rho}_i\right) + \bar{\rho}_i, \quad \beta_1 = \min\left(\frac{\bar{\rho}_i - \epsilon}{\bar{\rho}_i - \rho_{\min}}, 1\right). \tag{54}$$

In this way, the density values and slopes in the element are limited.

We then construct an intermediate state $\mathbf{u}^\star = (\rho^\star, \rho\mathbf{v}, \rho\mathbf{E})$. If the positivity of pressure is not satisfied, i.e., $p^\star < \epsilon$, the following nonlinear equation is solved at all the solution and flux points,

$$p\left(\beta_l \left(\mathbf{u}_{i,j,k}^\star - \overline{\mathbf{u}}_i\right) + \overline{\mathbf{u}}_i\right) = \epsilon, \tag{55}$$

where the corresponding slope restriction β_l can be obtained at different locations. The final limited solution at the j-th solution point and the k-th quadrature point is computed by

$$\mathbf{u}^{+}_{i,j,k} = \beta_2 \left(\mathbf{u}^{\star}_{i,j,k} - \bar{\mathbf{u}}_i \right) + \bar{\mathbf{u}}_i, \quad \beta_2 = \min_l \left(\beta_l \right). \tag{56}$$

This scheme guarantees that the density and pressure stay positive at the solution and flux points.

Let us now write down the process of the complete solution algorithm. For sake of readability, we assume a forward Euler time integration, while it is feasible to use other integrators. Considering the solution $\check{\mathbf{u}}_i^{N,n}$ and its average $\bar{\mathbf{u}}_i^n$ at time step t^n inside the standard element $\boldsymbol{\Omega}_i$, the solution algorithm yields,

$$\begin{aligned} \mathbf{u}_i^{N,+} &= \mathcal{P}(\mathbf{u}_i^{N,n}), \\ \mathbf{u}_i^{N,++} &= \mathbf{u}_i^{N,+} - \Delta t \nabla_{\mathbf{r}} \cdot \mathbf{f}_i^{N,+}, \\ \mathbf{u}_i^{N,n+1} &= \mathcal{F}(\mathbf{u}_i^{N,++}), \end{aligned} \tag{57}$$

Here, the limiting process including Eqs. (51), (54), (55), and (56) is denoted by $\mathcal{P}$, and the filtering step is denoted by $\mathcal{F}$. Note that for $\Delta x, \Delta t \to 0$, the solution algorithm is consistent with the hyperbolicity-preserving SG method [48].

5 Numerical Experiments

In this section, we will conduct numerical experiments to validate the current scheme. Dimensionless variables are introduced as follows,

$$\tilde{\mathbf{x}} = \frac{\mathbf{x}}{L_0}, \ \tilde{t} = \frac{t}{L_0/V_0}, \ \tilde{\mathbf{u}} = \frac{\mathbf{u}}{U_0},$$

where L_0 is the reference length, V_0 is the reference speed and U_0 denotes the reference conservative variables. For brevity, we drop the tilde notation to denote dimensionless variables henceforth. In all cases, the Gauss-Legendre rule is used to determine the solution collocation points in the reference space.

5.1 Advection Equation

In the first numerical experiment, we study the linear advection equation and validate the rate of convergence of the scheme. The one-dimensional wave propagation problem with random inputs is employed as the test case, i.e.,

$$\partial_t u + a \partial_x u = 0.$$

Two different kinds of uncertainty are considered.

5.1.1 Random Initial Condition

In this case, the initial condition is set as,

$$u(t = 0, x, \mathbf{z}) = \xi(\mathbf{z}) \sin(\pi x),$$

and the exact solution of the linear advection equation is,

$$u(t, x, \mathbf{z}) = \xi \sin(\pi(x - at)).$$

We consider the uniform distributed amplitudes in one- and two-dimensional random space, i.e.,

$$\xi = 1 + 0.1z_1,$$

and,

$$\xi = 1 + 0.1z_1 + 0.2z_2.$$

The Lagrange polynomials of degree 2 and 3 are employed in the computation. For the one-dimensional case, the auxiliary functions for the corrective fluxes are set to the Radau polynomials defined in Eq. (20) to recover the discontinuous Galerkin (DG) scheme, while Eq. (21) is employed in the two-dimensional case to recover the spectral difference (SD) scheme. The detailed computational setup is provided in Table 1. Following the criterion in Eq. (50), the filter is automatically turned off in this case.

Tables 2 and 3 list the numerical errors of expectation values and orders of convergence of the scheme under one-dimensional randomness. Tables 4 and 5 provide the corresponding results under two-dimensional randomness. It is clear that the current method preserves the desired third and fourth order of accuracy under different dimensions of uncertainty and correction functions. Figure 1 shows the expected value and standard deviation of the transport scalar u at $t = 50$ with 40 elements and 3 collocation points inside each cell under two-dimensional randomness. As shown, the long time behavior of the stochastic advection system is well captured.

5.1.2 Random Advection Velocity

In the second case, we test the convergence of the scheme with respect to the degree of polynomial chaos N_c. An advection velocity which follows a normal distribution is considered,

$$a \sim \mathcal{N}(1, 0.05).$$

Table 1 Computational setup of wave propagation problem with random initial condition

t	x	z_1	z_2	N_x	Points
(0, 50]	[−1, 1]	[−1, 1]	[−1, 1]	[4, 64]	Legendre
N_p	Correction	gPC	N_c	N_q	u_0
[3, 4]	Radau, SD	Legendre	5	100	$\xi \sin(\pi x)$
a	Flux	Integrator	Boundary	CFL	
1	Lax–Friedrichs	RK4	Periodic	0.1	

Table 2 Errors and rates of convergence of the third-order scheme in the wave propagation problem of the advection equation

Δx	L^1 error	Order	L^2 error	Order
0.5	5.941757E–2		1.960147E–2	
0.25	6.901634E–3	3.11	1.563457E–3	3.65
0.125	8.419116E–4	3.04	1.354328E–4	3.53
0.0625	1.045722E–4	3.01	1.191615E–5	3.51
0.03125	1.304139E–5	3.00	1.050922E–6	3.50

Table 3 Errors and rates of convergence of the fourth-order scheme in the wave propagation problem of the advection equation

Δx	L^1 error	Order	L^2 error	Order
0.5	7.184865E–3		1.912045E–3	
0.25	4.177470E–4	4.10	8.187982E–5	4.55
0.125	2.583430E–5	4.02	3.624978E–6	4.50
0.0625	1.619619E–6	4.00	1.635994E–7	4.47
0.03125	1.015061E–7	4.00	7.516612E–9	4.44

Table 4 Errors and rates of convergence of the third-order scheme in the wave propagation problem of the advection equation

Δx	L^1 error	Order	L^2 error	Order
0.5	6.508603E–2		2.691813E–2	
0.25	7.434318E–3	3.13	1.969617E–3	3.77
0.125	8.738582E–4	3.08	1.530354E–4	3.68
0.0625	1.073654E–4	3.02	1.222382E–5	3.65
0.03125	1.323275E–5	3.02	1.063807E–6	3.63

Table 5 Errors and rates of convergence of the fourth-order scheme in the wave propagation problem of the advection equation

Δx	L^1 error	Order	L^2 error	Order
0.5	7.255549E–3		2.081526E–3	
0.25	4.196887E–4	4.11	8.446775E–5	4.62
0.125	2.584450E–5	4.02	3.626445E–6	4.54
0.0625	1.621954E–6	3.99	1.604634E–7	4.50
0.03125	1.014556E–7	4.00	7.091867E–9	4.50

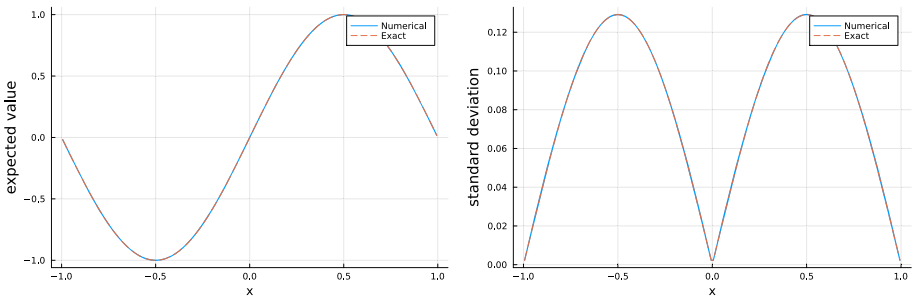

Fig. 1 The expected value (left) and standard deviation (right) of wave propagation problem with $N_x = 40$ at $t = 50$

The Hermite polynomial chaos is employed as the basis functions are defined on the random space $z \in [-\infty, \infty]$. The detailed computational setup is provided in Table 6.

Table 7 lists the numerical errors of both expectation values and standard deviations computed by the scheme with different gPC degree N_c. The spectral convergence of the stochastic Galerkin method can be clearly identified. Note that due to limited space and time resolution used in the scheme and the errors introduced by numerical quadrature in random space, the errors here do not reduce to machine precision.

Table 6 Computational setup of wave propagation problem with random advection velocity

t	x	z	N_x	Points	N_p
$(0, 50]$	$[-1, 1]$	$(-\infty, \infty)$	64	Legendre	4
Correction	gPC	N_c	N_q	u_0	a
Radau	Hermite	$[1, 6]$	100	$\sin(\pi x)$	$\mathcal{N}(1, 0.05)$
Flux	Integrator	Boundary	CFL		
Lax-Friedrichs	RK4	Periodic	0.1		

Table 7 Errors and rates of convergence of the fourth-order scheme in the wave propagation problem of the advection equation

N_c	L^1 error (mean)	L^2 error (mean)	L^1 error (std)	L^2 error (std)
1	6.058685E–3	3.434639E–4	7.626549E–2	4.323453E–3
2	6.053685E–5	3.431804E–6	5.284428E–3	4.019308E–4
3	7.313639E–7	4.162537E–8	1.044011E–4	6.213796E–6
4	7.293639E–7	4.134727E–8	3.470174E–6	2.649052E–7
5	7.270424E–7	4.121566E–8	2.426246E–7	1.420836E–8
6	7.270527E–7	4.121625E–8	2.316987E–7	1.297573E–8

5.2 Inviscid Burgers' Equation

Now let us shift our attention from capturing smooth solutions to tackling the problems where resolved and unresolved regions coexist. We first consider the inviscid Burgers' equation [45],

$$\partial_t u + u \partial_x u = 0.$$

Two random initial conditions are considered in one- and two-dimensional random space, respectively, i.e.,

$$u(t = 0, x, z_1) := \begin{cases} u_L, & \text{if } x < x_0 + \xi z_1, \\ u_M, & \text{if } x \in [x_0 + \xi z_1, x_1 + \xi z_1], \\ u_R, & \text{else}, \end{cases}$$

$$u_M = u_L + \frac{u_R - u_L}{x_0 - x_1} (x_0 + \xi z_1 - x),$$

and

$$u(t = 0, x, z_1, z_2) := \begin{cases} u_L, & \text{if } x < x_0 + \xi(z_1 + z_2), \\ u_M, & \text{if } x \in [x_0 + \xi(z_1 + z_2), x_1 + \xi(z_1 + z_2)], \\ u_R, & \text{else}, \end{cases}$$

$$u_M = u_L + \frac{u_R - u_L}{x_0 - x_1} (x_0 + \xi(z_1 + z_2) - x).$$

The detailed computational setup can be found in Table 8, where 17 and 289 quadrature points are used in one- and two-dimensional random space, respectively. The integrator denotes the Runge-Kutta pairs of order 5(4) proposed by Tsitouras [55] and $\{\varepsilon_1, \varepsilon_2\}$ are the parameters used to define the filter parameters in Eq. (41). Note that the Lasso filter does not

Table 8 Computational setup of Burgers shock problem

t	x	z_1	z_2	N_x	
$(0, 0.1]$	$[0, 3]$	$[-1, 1]$	$[-1, 1]$	100	
Points	N_p	Correction	u_L	u_R	
Legendre	$[4, 6]$	Radau	11	1	
x_0	x_1	ξ	gPC	N_c	
0.5	1.5	0.2	Legendre	9	
N_q	Flux	Integrator	Boundary	CFL	
$(17, 289)$	Lax-Friedrichs	Tsitouras	Dirichlet	0.1	
s_0	κ	ε_1	ε_2	α	s
$-2\log(N_p - 1)$	4	0.6	0.6	36	3

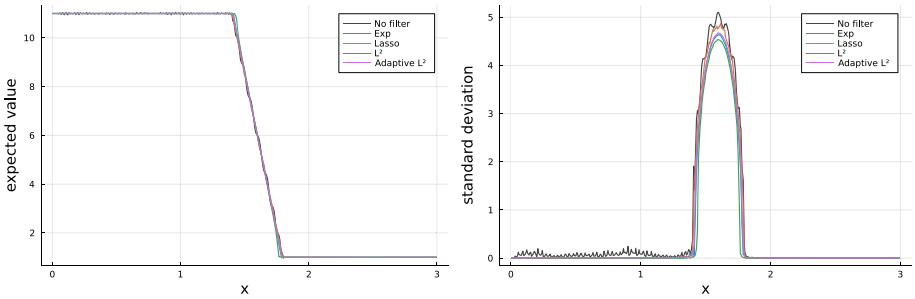

Fig. 2 The expected value (left) and standard deviation (right) of fourth-order Burgers' solutions at $t = 0.1$ with different filters

require these filter parameters as all parameters are chosen automatically. For the L^2 filter, a parameter study has been conducted to determine adequate values. The exponential filter uses the values from the study in Appendix A.

Figures 2 and 3 show the profiles of expected value and standard deviation at $t = 0.1$ with one-dimensional uncertainty computed by the fourth and sixth order schemes, respectively. As time goes, the initial solution moves through the physical domain and thereby forms an discontinuity. We compare the performance of different filters in this test case. For the standard SG method, the Gibbs phenomenon results in spurious oscillations. Compared to the expectation value, the variance is more sensitive and presents much stronger artifacts. As is shown, all the filters help mitigate that in the upstream region. In the shock region, all filters reduce oscillations, with the Lasso filter introducing the least numerical dissipation. The exponential filter and the L^2 filter show visibly more diffusive behavior. This introduction of numerical dissipation inevitably reduces the peak value of the standard deviations. However, benefiting from the discontinuity detector in Sect. 4.2, the adaptive L^2 filter results in a noticeable sharper profile while maintaining the robustness of the solution.

Figure 4 presents the results with two-dimensional uncertainty computed by the fourth order scheme. Although the higher dimensional random space exhibits a more significant Gibbs phenomenon, the filters effectively reduce the oscillation and stabilize the solution. The performance and numerical dissipation of different filters show the same pattern as in the one-dimensional case. This numerical experiment demonstrates the good performance of the Lasso filter and the adaptive filter, and thus we continue with them from now on.

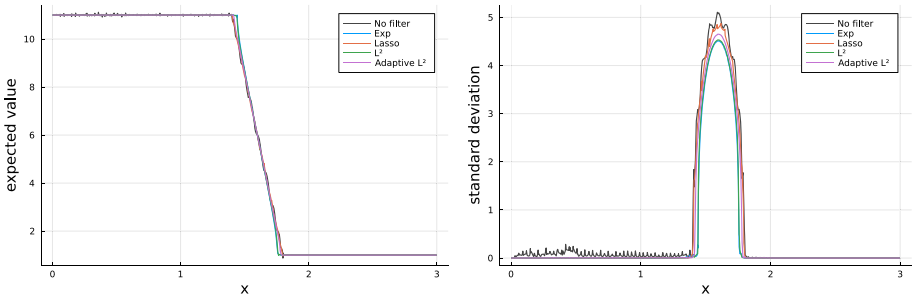

Fig. 3 The expected value (left) and standard deviation (right) of sixth-order Burgers' solutions at $t = 0.1$ with different filters

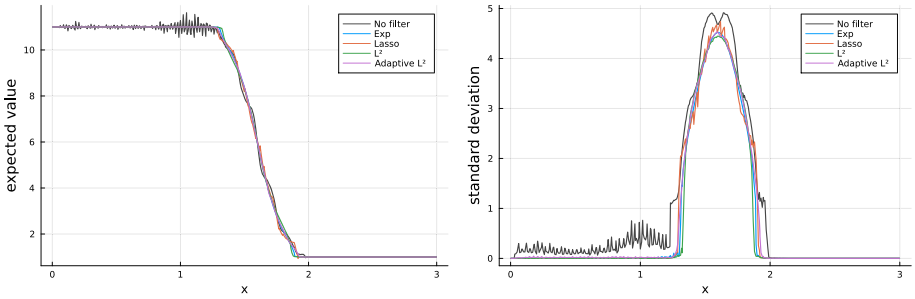

Fig. 4 The expected value (left) and standard deviation (right) of fourth-order Burgers' solutions at $t = 0.1$ with different filters

5.3 Euler Equations

5.3.1 Wave Propagation

As a more advanced test case, we turn to the one-dimensional Euler equations,

$$\frac{\partial}{\partial t}\begin{pmatrix}\rho\\ \rho U\\ \rho E\end{pmatrix}+\frac{\partial}{\partial x}\begin{pmatrix}\rho U\\ \rho U^2+p\\ (\rho E+p)U\end{pmatrix}=\begin{pmatrix}0\\0\\0\end{pmatrix}. \tag{58}$$

We first employ the propagation of a density wave as the benchmark to validate the rate of convergence of the current scheme for the nonlinear hyperbolic conservation laws. The initial condition with random input is set as,

$$\rho(t=0,x,z)=1+\frac{\xi(z)}{5}\sin(2\pi x),\ U=0,\ p=1.$$

With periodic boundary conditions, the exact solution of the Euler equations is as follows,

$$\rho(t,x,z)=\xi(z)\sin(2\pi(x-t)),\ U=0,\ p=1.$$

The computational setup is provided in Table 9.

The Lagrange polynomials of degree 3 are used in the simulation, which corresponds to the fourth-order scheme. Different number of elements from $N_x = 4$ to 64 are used to compute the rate of convergence. Following the criterion in Eq. (50), the filter is turned off

Table 9 Computational setup of the wave propagation problem for the Euler equations

t	x	z	N_x	Points	N_p
(0, 2]	[0, 1]	[−1, 1]	[4, 64]	Legendre	4
Correction	ξ	gPC	N_c	N_q	Flux
Raday	$\mathcal{U}(0.9, 1.1)$	Legendre	9	17	HLL
Integrator	Boundary	CFL			
Tsitouras	Periodic	0.1			

Table 10 Errors and convergences in the wave propagation problem of the Euler equations

Δx	L^1 error	Order	L^2 error	Order
0.25	7.148984E–4		1.908245E–4	
0.125	4.166900E–5	4.10	8.168646E–6	4.54
0.0625	2.581442E–6	4.01	3.609583E–7	4.50
0.03125	1.609450E–7	4.00	1.595023E–8	4.50
0.015625	1.005259E–8	4.00	7.048533E–10	4.50

automatically in this case. Table 10 shows the numerical errors and convergence orders. It is clear that the current scheme achieves the design accuracy.

5.3.2 Sod Shock Tube

We then consider the Riemann problem of the Euler equations with random inputs. For the Sod shock tube, the uncertainties are introduced by the stochastic initial conditions, i.e.,

$$\mathbf{v}(t=0,x,z) := \begin{pmatrix} \rho \\ U \\ p \end{pmatrix} = \begin{cases} \mathbf{v}_L, & x < x_c, \\ \mathbf{v}_R, & x \geq x_c, \end{cases} . \tag{59}$$

Following [63], we consider two types of initial discontinuities:

1. Stochastic density in the left-hand side,

$$\mathbf{v}_L = \begin{pmatrix} \xi \\ 0 \\ 1 \end{pmatrix}, \quad \mathbf{v}_R = \begin{pmatrix} 0.125 \\ 0 \\ 0.1 \end{pmatrix}, \quad x_c = 0.5, \tag{60}$$

2. Stochastic location of the initial discontinuity,

$$\mathbf{v}_L = \begin{pmatrix} 1 \\ 0 \\ 1 \end{pmatrix}, \quad \mathbf{v}_R = \begin{pmatrix} 0.125 \\ 0 \\ 0.1 \end{pmatrix}, \quad x_c = 0.5 + \sigma z. \tag{61}$$

The second case Eq. (61) is more challenging since the discontinuity is introduced in both physical and random space. As discussed in [46], a negative density or temperature induced by the gPC expansions may even lead to the failure of the solver at the first iterative step. The detailed computational setup can be found in Table 11.

For the first case of stochastic initial density, Eq. (60), the expected values and standard deviations of density, velocity and temperature inside the shock tube at $t = 0.15$ are shown in Fig. 5. The collocation results produced by the second-order finite volume method [61]

Table 11 Computational setup of Sod shock tube problem

t	x	z	N_x	Points	
(0, 0.15]	[0, 1]	[−1, 1]	100	Legendre	
N_p	Correction	ξ	σ	gPC	
3	Radau	$\mathcal{U}(0.9, 1.1)$	0.05	Legendre	
N_c	N_q	Flux	Integrator	Boundary	
9	17	HLL	Bogacki–Shampine	Dirichlet	
CFL	Filter	s_0	κ	ε_1	ε_2
0.1	(Lasso, L^2)	$-3\log 2$	4	0.6	(1, 0.6)

with 500 elements are plotted as benchmark. As can be seen, both filters robustly capture the expected structures of the rarefaction wave, the contact discontinuity and the shock wave. While the Lasso filter shows the least dissipative results, it exhibits some small oscillations close to the discontinuities of the standard deviations. The adaptive L^2 filter performs better with respect to the amount of oscillations, at the expense of a slightly more diffusive behavior. This is in agreement with the results of the filter comparison in Sect. 5.2.

In the second case, Eq. (61), shown in Fig. 6 the standard SG scheme fails within the beginning iterations due to the strong discontinuity in random space. The filters together with the positivity-preserving limiter play a good role in mitigating the oscillations and enabling the simulation. Similar as for the Burgers' equation in Sect. 5.2 and the previous test case, the Lasso filter presents less dissipation in the random space and thus results in sharper standard deviation values. The slight oscillations around the shock wave can be further dampened by the adaptive L^2 filter, as shown in Fig. 6, which is in agreement with the results of the filter comparison in Sect. 5.2.

5.3.3 Shock-Vortex Interaction

In the last case, we turn to the two-dimensional Euler equations,

$$\frac{\partial}{\partial t}\begin{pmatrix}\rho\\ \rho U\\ \rho V\\ \rho E\end{pmatrix}+\frac{\partial}{\partial x}\begin{pmatrix}\rho U\\ \rho U^2+p\\ \rho UV\\ (\rho E+p)U\end{pmatrix}+\frac{\partial}{\partial y}\begin{pmatrix}\rho U\\ \rho UV\\ \rho V^2+p\\ (\rho E+p)V\end{pmatrix}=\begin{pmatrix}0\\0\\0\\0\end{pmatrix}. \tag{62}$$

We consider the shock-vortex interaction problem, where longitudinal and transverse processes coexist in the flow domain under stochastic Mach numbers. The right-propagating shock wave is initialized by the Rankine-Hugoniot condition,

$$\begin{aligned}
&\rho_R=1,\ \rho_L=\frac{(\gamma+1)\mathrm{Ma}^2}{(\gamma-1)\mathrm{Ma}^2+2}\rho_R,\\
&U_R=0,\ U_L=c\mathrm{Ma}-\frac{(\gamma-1)\mathrm{Ma}^2+2}{(\gamma+1)\mathrm{Ma}^2},\\
&V_R=0,\ V_L=0,\\
&T_R=1,\ T_L=\frac{\left((\gamma-1)\mathrm{Ma}^2+2\right)\left(2\gamma\mathrm{Ma}^2-\gamma+1\right)}{(\gamma+1)^2\mathrm{Ma}^2}T_R,
\end{aligned} \tag{63}$$

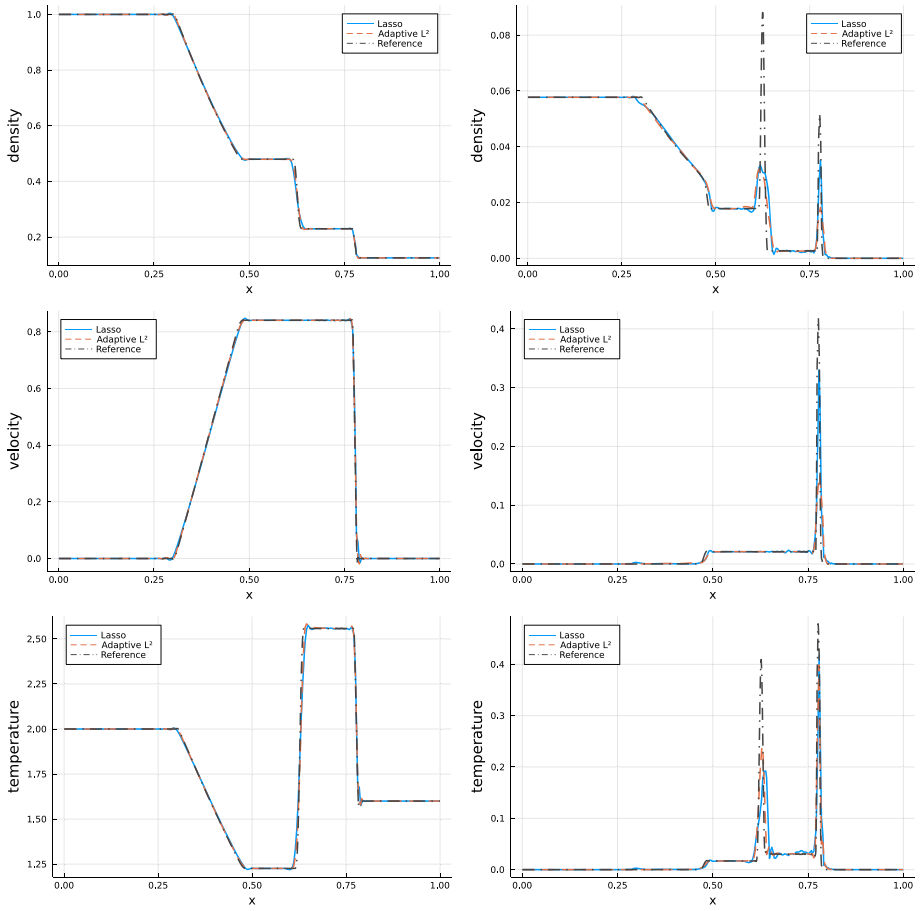

Fig. 5 The expected values (left column) and standard deviations (right column) of density, velocity and temperature in the Sod shock tube at $t = 0.15$ under stochastic initial density

where c is the speed of sound, and the variables with subscript R and L denote the upstream and downstream conditions, respectively. The specific heat ratio is denoted by γ and Ma is the Mach number. The vortex is defined as an isentropic perturbation to the background fluid,

$$\begin{aligned}(\delta U,\ \delta V) &= \zeta\eta e^{\mu(1-\eta^2)}(\sin\theta, -\cos\theta),\\ \delta T &= -\frac{(\gamma-1)\zeta^2}{4\mu\gamma}e^{2\mu(1-\eta^2)},\ \delta S = 0,\end{aligned} \tag{64}$$

where $S = \ln(p/\rho^\gamma)$ is the entropy. A polar coordinate (r, θ) is formulated by the center of the vortex (x_c, y_c) and $\eta = r/r_c$. The parameter κ defines the strength of the vortex, μ indicates the decay rate of the vortex, and r_c is the critical radius at which the vortex holds the maximum strength. The initial flow field is therefore set as,

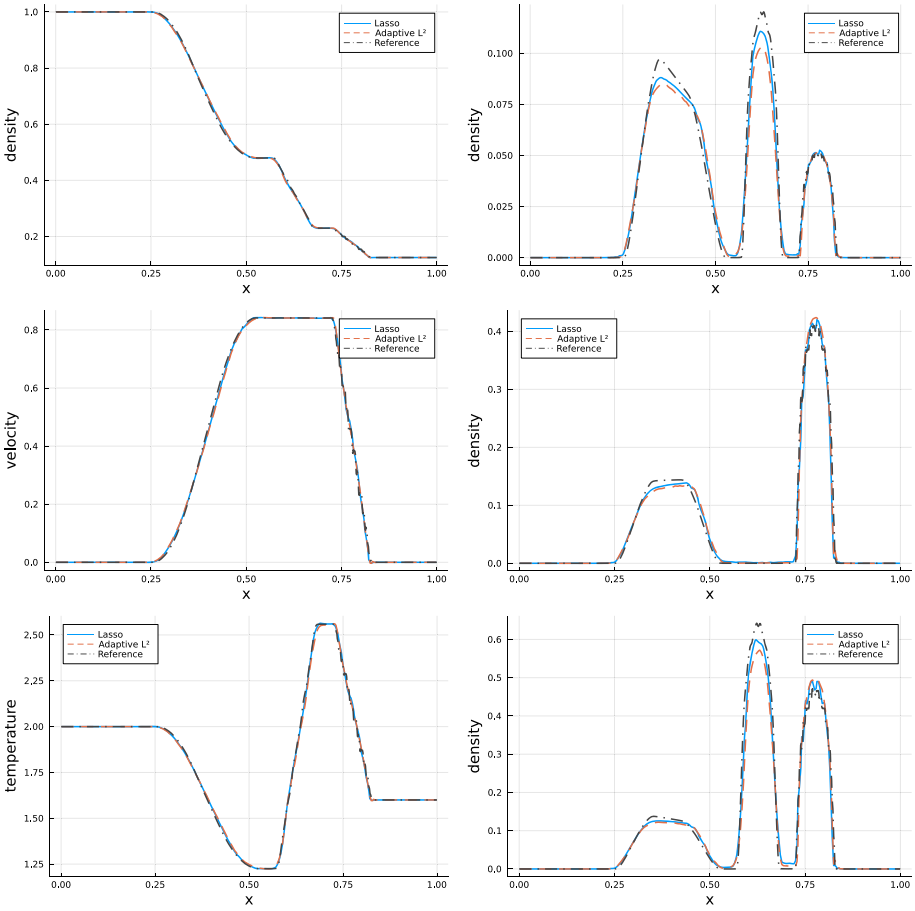

Fig. 6 The expected values (left column) and standard deviations (right column) of density, velocity and temperature in the Sod shock tube at $t = 0.15$ under stochastic initial discontinuity location

$$\mathbf{v}(t=0,x,y,z) := \begin{pmatrix} \rho \\ U \\ V \\ p \end{pmatrix} = \begin{cases} \mathbf{v}_L + \delta\mathbf{v}, & x < x_s, \\ \mathbf{v}_R + \delta\mathbf{v}, & x \geq x_s, \end{cases} \tag{65}$$

where x_s is the location of the shock. The detailed computational setup can be found in Table 12.

Figures 7, 8 and 9 present the expected values and standard deviations of density contours at $t = 0.3$, 0.5 and 0.7. As shown, the fine structures emerging from the interaction between longitudinal and transverse fluid processes are robustly captured by the current scheme. The roles of shock and vortex as source terms of uncertainties is clearly demonstrated. Figures 10 and 11 provide the profiles of density and temperature along the horizontal central line. The collocation results produced by the deterministic flux reconstruction method and the second-order finite volume method [61] with the same amount of elements are plotted for comparison. Benefiting from the higher-order representation, the accuracy and fidelity of solutions are improved compared to the collocation and the second-order finite volume results.

Table 12 Computational setup of shock-vortex interaction problem

t	x	y	z	N_x	N_y
(0, 1]	[0, 2]	[0, 1]	[−1, 1]	100	50
Points	N_p	Correction	Ma	x_s	x_c
Legendre	3	Radau	$\mathcal{U}(1.06, 1.18)$	0.25	0.8
y_c	r_c	ζ	μ	gPC	N_c
0.5	0.05	0.25	0.204	Legendre	5
N_q	Flux	Integrator	Boundary	CFL	Filter
9	HLL	Bogacki-Shampine	Reflection	0.1	L^2
s_0	κ	ε_1	ε_2		
$-3\log 2$	4	0.6	1		

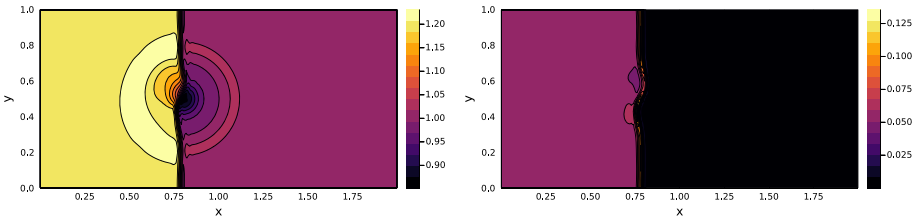

Fig. 7 Expected value (left) and standard deviation (right) of density in the shock-vortex interaction problem at $t = 0.3$

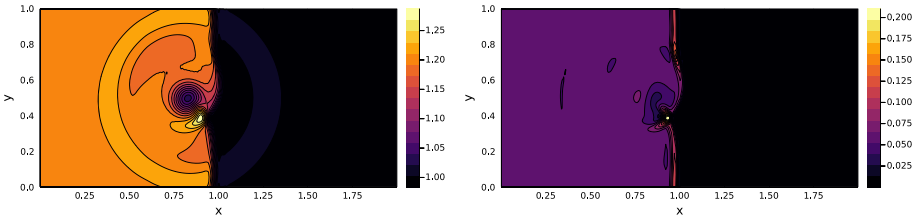

Fig. 8 Expected value (left) and standard deviation (right) of density in the shock-vortex interaction problem at $t = 0.5$

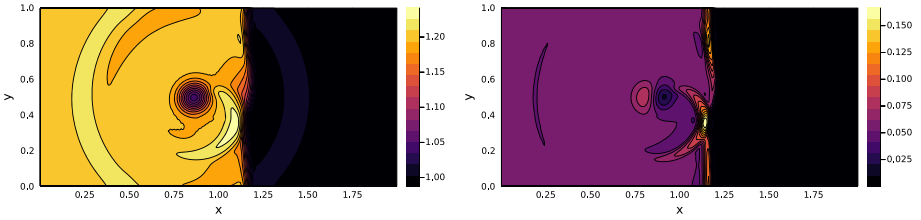

Fig. 9 Expected value (left) and standard deviation (right) of density in the shock-vortex interaction problem at $t = 0.7$

6 Conclusion

The development of higher-fidelity numerical schemes is crucial in computational fluid dynamics. In this paper, we present the first flux reconstruction stochastic Galerkin method for the study of uncertainty propagation. Benefiting from the uniform spectral discretiza-

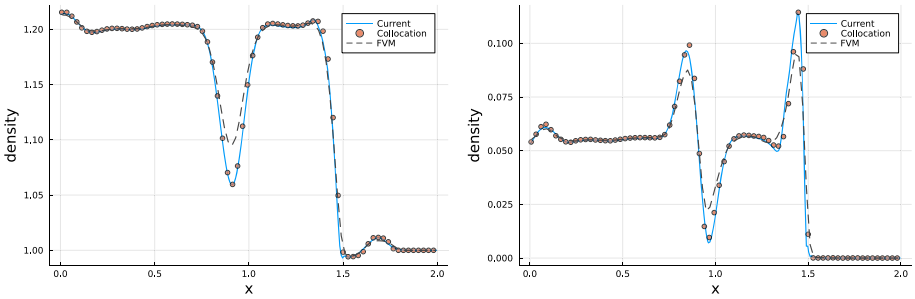

Fig. 10 Expected value (left) and standard deviation (right) of density in the shock-vortex interaction problem at $t = 1$

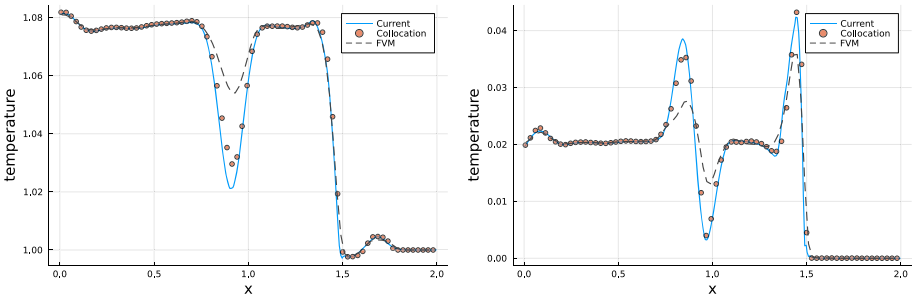

Fig. 11 Expected value (left) and standard deviation (right) of temperature in the shock-vortex interaction problem at $t = 1$

tion, an accurate approximation of solutions can be achieved, and the numerical behaviors of the scheme in spatial and random domain are consistent. The nodal and modal representations can be transformed naturally based on orthogonal polynomials and solution collocation points. A family of multi-dimensional filters is developed to mitigate the Gibbs phenomenon and a positivity-preserving limiter is employed to preserve physically realizable solutions. As a result, the current scheme is able to solve cross-scale problems, where resolved and unresolved regions coexist in the flow domain. It provides a powerful tool for the study of sensitivity analysis and uncertainty propagation, and the performance is demonstrated through numerical experiments.

For future work, it is possible to apply the scheme to other complex systems, e.g., astrophysics [62], particle transports [66], and plasma physics [63]. An alternative to a realizability-preserving limiter is the careful alteration of the SG system itself, such that its hyperbolicity domain is significantly enlarged, or possibly the whole space. This approach of deriving globally hyperbolic models has been successfully applied for kinetic equations and free-surface flows, see [6, 21, 31, 32]. A similar approach might be used in SG models to avoid using bound-preserving limiters in future work.

Author Contributions All authors contributed to the study conception and design. Material preparation, data collection and analysis were performed by Tianbai Xiao, Jonas Kusch and Julian Koellermeier. The first draft of the manuscript was written by Tianbai Xiao and all authors commented on previous versions of the manuscript. All authors read and approved the final manuscript.

Funding Tianbai Xiao is funded by the Alexander von Humboldt Foundation (Ref3.5-CHN-1210132-HFST-P). Jonas Kusch is funded by the Deutsche Forschungsgemeinschaft (DFG, German Research Foundation)

– Project-ID 258734477 – SFB 1173. The financial support of the CogniGron research center and the Ubbo Emmius Funds (University of Groningen) is acknowledged.

Data Availability The datasets generated and analysed during the current study are available from the corresponding author on reasonable request.

Declaration

Competing interests The authors have no relevant financial or non-financial interests to disclose.

A Appendix Parameter Choice for Exponential Filter

While the Lasso filter does not require numerical parameter choices, the exponential filter from Sect. 4.1.1 uses several parameters which need to be determined in applications Table (13).

Different strategies exist in the literature. In [26] the filter parameter is chosen as $\alpha = 36$, together with the filter exponent $s = 36$ to ensure that the last mode is damped to zero up to machine precision. However, the effect on the solution behavior is not clarified. In [31] the parameter choice was motivated with a number of heuristics. Firstly, the effect of the filter on the oscillation of the solution was investigated. Not surprisingly, it was found that larger parameters α smooth the solution and eventually recover positivity of the filtered distribution function. Secondly, a linear stability analysis of the model linearised around its equilibrium state revealed the damping factors for each mode. It was shown that the choice $\alpha = 36$ leads to small damping (i.e., less added diffusion) of the solution, while completely damping out the fastest mode. Lastly, the filter was tested with different parameters for the full model and the value $\alpha = 36$ indeed performed best with respect to the solution quality. While the best choice might depend on the size of the model, the choice of $\alpha = 36$ was robust in the test cases computed in [31] and this value was therefore used for all further tests computed therein.

In the context of the SG models here, a similar parameter study can be performed to determine a suitable value for the filter parameter. Figure 12 shows the expectation and standard deviation for a simple Burger's equation test case and different filter parameters α. We choose a constant $s = 3$ as the filter exponent s is only modifying the shape of the filter strength in a mild way. Furthermore, we also choose $N^* = 0$ fixed as no additional variables need to remain unchanged.

The results in Fig. 12 clearly visualize that a small value of the filter parameter α, e.g., $\alpha = 1$, is not sufficient to damp the oscillations of both the expected values as well as the standard deviation. Similarly, a very large value of the filter parameter, e.g., $\alpha = 60, 100$, also leads to oscillations. In between, there is a range of parameters, for which the oscillations become negligible. This includes the value $\alpha = 36$, which was frequently used in the literature. This indicates that the choice of $\alpha = 36$ also seems to perform well in the settings of this paper and we therefore use it in all test cases including the exponential filter.

Table 13 Nomenclature

$t, \mathbf{x}, \mathbf{z}$	time, space and random variables
$\mathbf{u}$	conservative variable
$\mathbf{f}$	flux function
N_c	degree of polynomial chaos
$\mathbf{u}^{N_c}$	spectral approximation of $\mathbf{u}$, i.e., $\sum_{\|k\|=0}^{N_c} \hat{\mathbf{u}}_k \Phi_k$
$\hat{\boldsymbol{v}}$	matrix form of gPC coefficients of conservative variables, i.e., $\{\hat{\mathbf{u}}_k, \|k\| \leq N_c\}$
$\boldsymbol{\Phi}$	orthogonal polynomial basis in random space
ϱ	probability density function
N_q	number of quadrature points in random space
$\boldsymbol{\Omega}$	physical space
$\mathbf{r}$	coordinates in the reference space of standard element
$\boldsymbol{\Theta}$	transformation function of coordinates, i.e., $\mathbf{x} = \boldsymbol{\Theta}(\mathbf{r})$
$\hat{\boldsymbol{v}}^{\delta}$	matrix form of gPC coefficients of conservative variables in the reference space
ℓ	Lagrange polynomials
N_p	number of solution points
J	Jacobian of coordinate transformation
$\hat{\boldsymbol{f}}^{\delta}$	matrix form of gPC coefficients of fluxes in the reference space
$\hat{\boldsymbol{f}}^{\delta D}$	discontinuous fluxes in the reference space
$\hat{\boldsymbol{f}}^{\delta C}$	corrective fluxes in the reference space
$\hat{\boldsymbol{f}}^{\delta I}$	interactive fluxes in the reference space
h_L, h_R	auxiliary functions for corrective fluxes
L_k	Legendre polynomial of degree k
H	Heaviside step function
$\hat{\boldsymbol{F}}^{\delta}$	two-dimensional fluxes for gPC coefficients in the reference space
$\mathbf{h}$	auxiliary function for two-dimensional corrective fluxes
$\boldsymbol{\Psi}$	orthogonal polynomial basis in physical space
$\mathbf{u}^{N}$	nodal representation of the solution
$\tilde{\mathbf{u}}^{N}$	modal representation of the solution
$\mathcal{V}$	Vandermonde matrix
$\mathcal{F}$	filter function
$\mathbf{u}^{*}$	post-filter solution
N^{*}	cut-off order of exponential filter
λ	filter strength
Λ	matrix of filter strength whose entries are λ
$\circ$	abbreviation of filter operator
$\mathcal{L}$	penalty operator of solution oscillation
α_1, α_2	filter-specific parameters

Table 13 continued

$\mathbf{S}_e$	slope indicator in which the first state is denoted as S_e
s_0, s_e	parameters in the discontinuity detector
θ	discontinuity detector
$\beta_1, \beta_2, \beta_l$	parameters in the positivity-preserving limiter

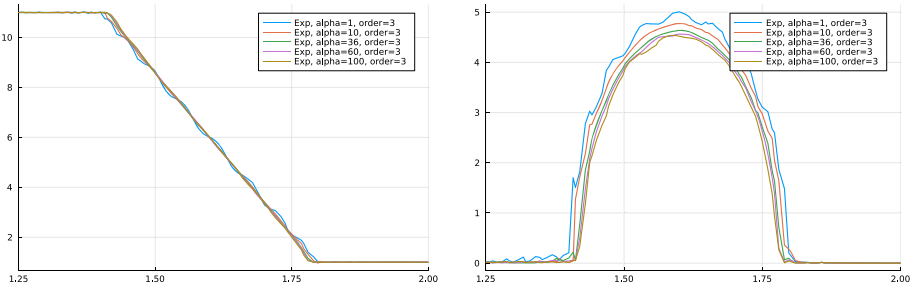

(a) Expectation (b) Standard deviation

Fig. 12 Expected value and standard deviation for Burger's equation and varying filter parameters α of the exponential filter. The filter exponent is kept fixed at $s = 3$ and we choose $N_* = 0$

References

1. Abgrall, R., Mishra, S.: Uncertainty quantification for hyperbolic systems of conservation laws. In: Handbook of Numerical Analysis, vol. 18, pp. 507–544. Elsevier (2017)
2. Alldredge, G., Frank, M., Kusch, J., McClarren, R.: A realizable filtered intrusive polynomial moment method. arXiv preprint arXiv:2105.07473 (2021)
3. Barth, T.J., Deconinck, H.: High-Order Methods for Computational Physics, vol. 9. Springer (2013)
4. Buerger, R., Kroeker, I., Rohde, C.: A hybrid stochastic Galerkin method for uncertainty quantification applied to a conservation law modelling a clarifier-thickener unit (2014)
5. Burbeau, A., Sagaut, P., Bruneau, C.H.: A problem-independent limiter for high-order runge-kutta discontinuous galerkin methods. J. Comput. Phys. **169**(1), 111–150 (2001)
6. Cai, Z., Fan, Y., Li, R.: Globally hyperbolic regularization of grad's moment system in one dimensional space. Commun. Math. Sci. **11**(2), 547–571 (2013). https://doi.org/10.4310/CMS.2013.v11.n2.a12
7. Canuto, C., Quarteroni, A.: Approximation results for orthogonal polynomials in sobolev spaces. Math. Comput. **38**(157), 67–86 (1982)
8. Chertock, A., Jin, S., Kurganov, A.: An operator splitting based stochastic galerkin method for the one-dimensional compressible euler equations with uncertainty. Preprint pp. 1–21 (2015)
9. Chertock, A., Jin, S., Kurganov, A.: A well-balanced operator splitting based stochastic galerkin method for the one-dimensional saint-venant system with uncertainty. Preprint (2015)
10. Cockburn, B., Karniadakis, G.E., Shu, C.W.: Discontinuous Galerkin Methods: Theory, Computation and Application, vol. 11. Springer (2012)
11. Cox, C., Trojak, W., Dzanic, T., Witherden, F., Jameson, A.: Accuracy, stability, and performance comparison between the spectral difference and flux reconstruction schemes. Comput. Fluids **221**, 104922 (2021)
12. Dai, D., Epshteyn, Y., Narayan, A.: Hyperbolicity-preserving and well-balanced stochastic galerkin method for shallow water equations. SIAM J. Sci. Comput. **43**(2), A929–A952 (2021)
13. Dai, D., Epshteyn, Y., Narayan, A.: Hyperbolicity-preserving and well-balanced stochastic galerkin method for two-dimensional shallow water equations. J. Comput. Phys. **452**, 110901 (2022)
14. De Grazia, D., Mengaldo, G., Moxey, D., Vincent, P., Sherwin, S.: Connections between the discontinuous Galerkin method and high-order flux reconstruction schemes. Int. J. Numer. Meth. Fluids **75**(12), 860–877 (2014)

15. Després, B., Poëtte, G., Lucor, D.: Robust uncertainty propagation in systems of conservation laws with the entropy closure method. In: Uncertainty quantification in computational fluid dynamics, pp. 105–149. Springer (2013)
16. Di, Y., Fan, Y., Kou, Z., Li, R., Wang, Y.: Filtered hyperbolic moment method for the vlasov equation. J. Sci. Comput. (2018). https://doi.org/10.1007/s10915-018-0882-8
17. Donoghue, G., Yano, M.: Spatio-stochastic adaptive discontinuous galerkin methods. Comput. Methods Appl. Mech. Eng. **374**, 113570 (2021)
18. Dürrwächter, J., Kuhn, T., Meyer, F., Schlachter, L., Schneider, F.: A hyperbolicity-preserving discontinuous stochastic galerkin scheme for uncertain hyperbolic systems of equations. J. Comput. Appl. Math. **370**, 112602 (2020)
19. Dürrwächter, J., Meyer, F., Kuhn, T., Beck, A., Munz, C.D., Rohde, C.: A high-order stochastic galerkin code for the compressible euler and navier-stokes equations. Comput. Fluids 105039 (2021)
20. Fan, Y., Koellermeier, J.: Accelerating the convergence of the moment method for the Boltzmann equation using filters. J. Sci. Comput. **84**(1), 1–28 (2020). https://doi.org/10.1007/s10915-020-01251-8
21. Fan, Y., Koellermeier, J., Li, J., Li, R., Torrilhon, M.: Model reduction of kinetic equations by operator projection. J. Stat. Phys. **162**(2), 457–486 (2016). https://doi.org/10.1007/s10955-015-1384-9
22. Gerster, S., Herty, M.: Entropies and symmetrization of hyperbolic stochastic Galerkin formulations. Commun. Comput. Phys. **27**(639–671), 1 (2020)
23. Gerster, S., Herty, M., Sikstel, A.: Hyperbolic stochastic Galerkin formulation for the p-system. J. Comput. Phys. **395**, 186–204 (2019)
24. Giles, M.B.: Multilevel Monte Carlo methods. Acta Numer. **24**, 259–328 (2015)
25. Hesthaven, J.S., Warburton, T.: Nodal Discontinuous Galerkin Methods: Algorithms, Analysis, and Applications. Springer (2007)
26. Hou, T.Y., Li, R.: Computing nearly singular solutions using pseudo-spectral methods. J. Comput. Phys. **226**(1), 379–397 (2007)
27. Hu, J., Jin, S., Shu, R.: On stochastic Galerkin approximation of the nonlinear Boltzmann equation with uncertainty in the fluid regime. J. Comput. Phys. **397**, 108838 (2019)
28. Huynh, H.T.: A flux reconstruction approach to high-order schemes including discontinuous Galerkin methods. In: 18th AIAA Computational Fluid Dynamics Conference, p. 4079 (2007)
29. Jin, S., Xiu, D., Zhu, X.: Asymptotic-preserving methods for hyperbolic and transport equations with random inputs and diffusive scalings. J. Comput. Phys. **289**, 35–52 (2015)
30. Knio, O.M., Najm, H.N., Ghanem, R.G., et al.: A stochastic projection method for fluid flow: I. Basic formulation. J. Comput. Phys. **173**(2), 481–511 (2001)
31. Koellermeier, J., Rominger, M.: Analysis and numerical simulation of hyperbolic shallow water moment equations. Commun. Comput. Phys. **28**(3), 1038–1084 (2020)
32. Koellermeier, J., Schaerer, R.P., Torrilhon, M.: A framework for hyperbolic approximation of kinetic equations using quadrature-based projection methods. Kinet. Rel. Models **7**(3), 531–549 (2014). https://doi.org/10.3934/krm.2014.7.531
33. Kopriva, D.A., Kolias, J.H.: A conservative staggered-grid Chebyshev multidomain method for compressible flows. J. Comput. Phys. **125**(1), 244–261 (1996)
34. Kusch, J., Alldredge, G.W., Frank, M.: Maximum-principle-satisfying second-order intrusive polynomial moment scheme. SMAI J. Comput. Math. **5**, 23–51 (2019)
35. Kusch, J., McClarren, R.G., Frank, M.: Filtered stochastic Galerkin methods for hyperbolic equations. J. Comput. Phys. **403**, 109073 (2020)
36. Kusch, J., Schlachter, L.: Oscillation mitigation of hyperbolicity-preserving intrusive uncertainty quantification methods for systems of conservation laws. J. Comput. Appl. Math. 113714 (2021)
37. Kusch, J., Wolters, J., Frank, M.: Intrusive acceleration strategies for uncertainty quantification for hyperbolic systems of conservation laws. J. Comput. Phys. **419**, 109698 (2020)
38. Le Maitre, O., Knio, O., Najm, H., Ghanem, R.: Uncertainty propagation using Wiener–Haar expansions. J. Comput. Phys. **197**(1), 28–57 (2004)
39. Liu, Y., Vinokur, M., Wang, Z.J.: Spectral difference method for unstructured grids I: basic formulation. J. Comput. Phys. **216**(2), 780–801 (2006)
40. Meyer, F., Rohde, C., Giesselmann, J.: A posteriori error analysis for random scalar conservation laws using the stochastic Galerkin method. IMA J. Numer. Anal. **40**(2), 1094–1121 (2020)
41. Öffner, P., Glaubitz, J., Ranocha, H.: Stability of correction procedure via reconstruction with summation-by-parts operators for burgers' equation using a polynomial chaos approach. ESAIM: Math. Model. Numer. Anal. **52**(6), 2215–2245 (2018)
42. Persson, P.O., Peraire, J.: Sub-cell shock capturing for discontinuous Galerkin methods. In: 44th AIAA Aerospace Sciences Meeting and Exhibit, p. 112 (2006)

43. Pettersson, P., Iaccarino, G., Nordström, J.: Numerical analysis of the Burgers' equation in the presence of uncertainty. J. Comput. Phys. **228**(22), 8394–8412 (2009)
44. Pettersson, P., Iaccarino, G., Nordström, J.: A stochastic galerkin method for the euler equations with roe variable transformation. J. Comput. Phys. **257**, 481–500 (2014)
45. Poëtte, G., Després, B., Lucor, D.: Uncertainty quantification for systems of conservation laws. J. Comput. Phys. **228**(7), 2443–2467 (2009). https://doi.org/10.1016/j.jcp.2008.12.018
46. Poëtte, G., Després, B., Lucor, D.: Uncertainty quantification for systems of conservation laws. J. Comput. Phys. **228**(7), 2443–2467 (2009)
47. Rajput, M.M.: Master thesis filtered stochastic Galerkin for radiative transfer and fluid dynamics. Master thesis, Karlsruhe Institute of Technology (2020)
48. Schlachter, L., Schneider, F.: A hyperbolicity-preserving stochastic Galerkin approximation for uncertain hyperbolic systems of equations. J. Comput. Phys. **375**, 80–98 (2018)
49. Smith, R.C.: Uncertainty quantification: theory, implementation, and applications, vol. 12. SIAM (2013)
50. Sousedík, B., Elman, H.C.: Stochastic Galerkin methods for the steady-state Navier–Stokes equations. J. Comput. Phys. **316**, 435–452 (2016)
51. Tibshirani, R.: Regression shrinkage and selection via the lasso. J. Roy. Stat. Soc.: Ser. B (Methodol.) **58**(1), 267–288 (1996)
52. Toro, E.F.: Riemann Solvers and Numerical Methods for Fluid Dynamics: A Practical Introduction. Springer (2013)
53. Tryoen, J., Le Maitre, O., Ndjinga, M., Ern, A.: Intrusive Galerkin methods with upwinding for uncertain nonlinear hyperbolic systems. J. Comput. Phys. **229**(18), 6485–6511 (2010)
54. Tryoen, J., Le Maitre, O.L., Ern, A.: Adaptive anisotropic spectral stochastic methods for uncertain scalar conservation laws. SIAM J. Sci. Comput. **34**(5), A2459–A2481 (2012)
55. Tsitouras, C.: Runge–Kutta pairs of order 5 (4) satisfying only the first column simplifying assumption. Comput. Math. Appl. **62**(2), 770–775 (2011)
56. Vandenhoeck, R., Lani, A.: Implicit high-order flux reconstruction solver for high-speed compressible flows. Comput. Phys. Commun. **242**, 1–24 (2019)
57. Vincent, P.E., Castonguay, P., Jameson, A.: A new class of high-order energy stable flux reconstruction schemes. J. Sci. Comput. **47**(1), 50–72 (2011)
58. Wan, X., Karniadakis, G.E.: Multi-element generalized polynomial Chaos for arbitrary probability measures. SIAM J. Sci. Comput. **28**(3), 901–928 (2006)
59. Wang, Z.J., Fidkowski, K., Abgrall, R., Bassi, F., Caraeni, D., Cary, A., Deconinck, H., Hartmann, R., Hillewaert, K., Huynh, H.T., et al.: High-order cfd methods: current status and perspective. Int. J. Numer. Meth. Fluids **72**(8), 811–845 (2013)
60. Wu, K., Tang, H., Xiu, D.: A stochastic Galerkin method for first-order quasilinear hyperbolic systems with uncertainty. J. Comput. Phys. **345**, 224–244 (2017)
61. Xiao, T.: Kinetic.jl: A portable finite volume toolbox for scientific and neural computing. J. Open Source Softw. **6**(62), 3060 (2021)
62. Xiao, T., Cai, Q., Xu, K.: A well-balanced unified gas-kinetic scheme for multiscale flow transport under gravitational field. J. Comput. Phys. **332**, 475–491 (2017)
63. Xiao, T., Frank, M.: A stochastic kinetic scheme for multi-scale flow transport with uncertainty quantification. J. Comput. Phys. **437**, 110337 (2021)
64. Xiao, T., Frank, M.: A stochastic kinetic scheme for multi-scale plasma transport with uncertainty quantification. J. Comput. Phys. **432**, 110139 (2021)
65. Xiao, T., Kusch, J., Koellermeier, J.: FRSG: stochastic Galerkin method with flux reconstruction. https://github.com/CSMMLab/FRSG (2021). https://doi.org/10.5281/zenodo.5588317
66. Xiao, T., Liu, C., Xu, K., Cai, Q.: A velocity-space adaptive unified gas kinetic scheme for continuum and rarefied flows. J. Comput. Phys. **415**, 109535 (2020)
67. Xiu, D.: Numerical Methods for Stochastic Computations: A Spectral Method Approach. Princeton University Press (2010)
68. Xiu, D., Karniadakis, G.E.: Modeling uncertainty in flow simulations via generalized polynomial chaos. J. Comput. Phys. **187**(1), 137–167 (2003)
69. Yu, M., Wang, Z.J., Liu, Y.: On the accuracy and efficiency of discontinuous Galerkin, spectral difference and correction procedure via reconstruction methods. J. Comput. Phys. **259**, 70–95 (2014)
70. Zhong, X., Shu, C.W.: Entropy stable Galerkin methods with suitable quadrature rules for hyperbolic systems with random inputs. J. Sci. Comput. **92**(1), 1–30 (2022)